

PALAIOS, 2017, v. 32, 600–619 Research Article DOI: http://dx.doi.org/10.2110/palo.2017.011



TAPHONOMIC ANALYSIS OF CAMBRIAN VERMIFORM FOSSILS OF UTAH AND NEVADA, AND IMPLICATIONS FOR THE CHEMISTRY OF BURGESS SHALE-TYPE PRESERVATION

JESSE S. BROCE AND JAMES D. SCHIFFBAUER

Department of Geological Sciences, University of Missouri, 101 Geology Building, Columbia, Missouri, 65211, USA email: schiffbauerj@missouri.edu

ABSTRACT: Burgess Shale-type preservation is a predominantly Paleozoic style of exceptional fossilization via the process of kerogenization, through which organic tissues are converted to more geologically stable forms of carbon. It is often associated with two additional modes of mineralization: (1) pyritization, collectively the precipitation of pyrite on, near, or replacing decaying organic matter; and (2) aluminosilicification, the association of clay minerals, frequently templating the fossil material. Further, some organisms preserved through the Burgess Shale-type pathway also show limited phosphatization, the replication of tissues by apatite, which is usually restricted to digestive tracts/organs. Here, sixteen Cambrian vermiform (worm-like) fossils, preserved via Burgess Shale-type preservation in three formations of the Great Basin, western US, were analyzed using scanning electron microscopy-based methodologies. These fossils display a wide range of taphonomic character, with visual differences in kerogenous-, pyrite-, and aluminosilicate-associated preservation, in addition to some preserved medial structures presumed to be gut tracts. Microchemical analyses indicate additional unique mineral associations, including barite and monazite, which can be broadly attributed to later-stage diagenetic alteration of the initial preservational mineralization. A consistent model of the chronology and drivers of mineralization is presented, and may prove useful for considering Burgess Shale-type preservation at other localities.

INTRODUCTION

The fossil record is principally comprised of the mineralized hard parts of deceased organisms. While much can be learned from skeletal remains, the characteristics of soft tissues provide distinctive biological value. Soft tissues degrade readily in most environments; however, under certain conditions, soft tissues can be preserved, typically proceeding via mineral replacement. Analysis of these 'exceptional' fossils can yield a wealth of information about the biology and physiology of the once living organism. Some degree of information loss is inevitable in any taphonomic scenario (e.g., Sansom et al. 2010), but deposits of exceptionally preserved fossils (Konservat-Lagerstätten, sec. Seilacher 1970) offer the best hope of a comprehensive understanding of ancient biology and ecology (Muscente et al. 2017)

The Burgess Shale, Canadian Rockies, is one of the most recognized fossil Lagerstätten, and exemplifies fossil preservation via compression of carbonaceous materials. Broadly recognized as Burgess Shale-type (BST) preservation (Butterfield 2003), this taphonomic mode also includes various mineral associations, such as clay mineral surface templates (e.g., Orr et al. 1998), anatomically restricted pyrite (e.g., Gabbott et al. 2004), and phosphatized gastrointestinal systems (e.g., Butterfield 2002; Lerosey-Aubril et al. 2012). In large part, this is because the range of environmental conditions that favor preservation of carbonaceous compressions (rapid burial to low energy, oxygen-limited systems) can also favor the formation of various accessory minerals, even though they form via different mechanisms and may require different geochemical settings (e.g., Anderson et al. 2011; Cai et al. 2012; Farrell 2014). The common association of such accessory minerals, especially pyrite and clay minerals, should perhaps be considered as facultative, but possibly facilitating, components of the BST preservational mode (Cai et al. 2012). Collectively, along with kerogenization of carbonaceous tissues, pyritization, aluminosilicification, and phosphatization may therefore contribute to a broader definition of the BST preservational pathway. The variability within the general theme of BST preservation has been extensively studied from a global distribution of sites, including such localities as the Burgess Shale proper (Orr et al. 1998), the Emu Bay Shale (Briggs and Nedin 1997), the Latham Shale (Briggs and Mount 1982), the Maotianshan Shale (Chengjiang biota) (Gabbott et al. 2004; Zhu et al. 2005; Forchielli et al. 2014), the Kaili Formation (Lin and Briggs 2010), and the Kinzers Formation (Skinner 2005), among numerous others—as well as many non-Cambrian sites with analogous preservation (Muscente et al. 2017).

BST Taphonomic Processes: Kerogenization

The kerogen in a BST fossil is generally comprised of remnant organic carbon from the tissues of the preserved organism. In most burial settings, however, organic tissues are prime electron donors for heterotrophic/ organotrophic microbial consumption. Thus, in order for these tissues to enter the fossil record as kerogen, they must have avoided significant microbially induced decay. However, even in cases of extreme carbon loss via microbial degradation, some large biopolymers, such as chitin and long-chain fatty acids, generally remain intact, owing to difficulties of assimilating/metabolizing these compounds by many microorganisms (Briggs et al. 2000). During diagenesis, the volatile components of such large biopolymers are lost (Bernard and Horsfield 2014), leaving behind remnant carbon compounds as solid, amorphous, inert kerogen. Kerogen is effectively a trash-can grouping of organic compounds that, with varying influences of time, increased burial, and thermal alteration, will undergo isomerization and aromatization into more ordered carbon-bearing compounds with strong carbon-carbon covalent bonds (e.g., Schopf et al. 2005; Schiffbauer et al. 2012). This alteration eventually results in

Published Online: September 2017

immobile and non-reactive products like pyrobitumen, as observed in overmature shales such as those in the House Range, Utah (Muscio and Horsfield 1996). Pyrolysis experiments additionally show that modern chitin-protein-lipid complexes seem likely to convert to stable aliphatic biopolymers during artificial thermal maturation over short experimental durations (Gupta et al. 2006). From the above described observations of both the fossil record and maturation experiments, one can surmise that it is possible, if not probable, that certain histological biochemistries are more likely to yield inert kerogen than others through their taphonomic history.

BST Taphonomic Processes: Pyritization

The taphonomic occurrence of pyritization is common in the fossil record (Farrell 2014), and typically manifests as either the complete, pervasive replacement of tissues by pyrite, or the precipitation of pyrite on tissues or in sediment immediately near tissues (Gabbott et al. 2004; Cai et al. 2012; Schiffbauer et al. 2014). Pyritization results from degradation of organic carbon by sulfate-reducing bacteria (SRBs), which yield bisulfide (HS⁻) ions as a product of their metabolism (Schiffbauer et al. 2014). Reduced iron is also required to form iron sulfide, presumed to be sourced from ambient sediment and pore water in the burial environment or from iron-reducing bacterial conversion of Fe3+ to Fe2+ (Farrell 2014). Pyritization requires anoxia, at least in a local microenvironment near the fossil. Not only are both sulfate-reducing and iron-reducing bacteria typically obligate anaerobes, but also, HS- and Fe2+ ions are rapidly converted to sulfate and ferric iron oxides/oxyhydroxides, respectively, in the presence of oxygen. Sulfide and ferrous iron react to form an iron monosulfide, either precipitating as solid mackinawite or remaining as aqueous FeS, which can be later converted to pyrite with an electron acceptor or via reaction with polysulfide (S_n²⁻) (Berner 1984; Hunger and Benning 2007). While pyrite is kinetically inhibited from nucleating without a substrate (Rickard and Luther III 2007), microorganisms have been shown in laboratory experiments to nucleate iron monosulfides as a result of the tendency of iron to adsorb to microbial cell walls (Konhauser 1998). In turn, this adsorption of iron serves to provide nucleation sites for, and increase the rate of, iron monosulfide precipitation, which subsequently transitions to pyrite and can continue to grow from aqueous sulfides and Fe²⁺ (Donald and Southam 1999; Petrovich 2001).

BST Taphonomic Processes: Aluminosilicification

While the progression of pyritization and its preservational role are relatively well-understood (e.g., Canfield and Raiswell 1991; Briggs et al. 1996; Schiffbauer et al. 2014), the same cannot be said for the formation or taphonomic function of associated clay minerals (e.g., Butterfield 1995; Orr et al. 1998; Petrovich 2001; Powell 2003; Gaines et al. 2008; Page et al. 2008; Anderson et al. 2011; Cai et al. 2012; Forchielli et al. 2012; Wilson and Butterfield 2014; McMahon et al. 2016). Clay minerals are known to be associated with many BST fossils, and in many cases appear to form an intimate textural relationship with fossil surfaces (Butterfield 1995; Orr et al. 2009). Clay minerals associated with fossils commonly have differing compositions than those of the host rock, frequently with higher iron or magnesium content (Orr et al. 1998). These compositional differences may reflect authigenic precipitation or early diagenetic alteration (Petrovich 2001; Gaudin et al. 2005; Cai et al. 2012), or alternatively, later metamorphic alteration (Powell 2003). While several studies suggest that fossil-associated clays serve no taphonomic role (Powell 2003; Gaines et al. 2008; Page et al. 2008), others have suggested positive effects of clays on the preservation of organic matter. Specifically, clays have been proposed to be taphonomically constructive: (1) by replicating or sealing fossil organisms (Orr et al. 1998); (2) by inactivating degradational/autolytic enzymes (Butterfield 1995; Forchielli et al. 2014); (3) by inhibiting the growth of bacterial decomposers (McMahon et al. 2016); and (4) by promoting a natural tanning process when present in the sediment (Wilson and Butterfield 2014).

BST Taphonomic Processes: Phosphatization

Phosphatization is notably different than the mineralization pathways reviewed above. Instead of being associated with the exterior of fossils, it is more commonly the gut tracts (and/or midgut glands) of organisms that are preserved in some BST localities as calcium phosphate (e.g., Butterfield 2002; Lerosey-Aubril et al. 2012). While the highly specific location (the digestive tract) is unique to this mineralization mode, the process of phosphatization is broadly attributed to the activity of microbes (Wilby and Briggs 1997; Raff et al. 2008; Raff and Raff 2014; Muscente et al. 2015).

GEOLOGIC SETTINGS

The specimens analyzed here were collected from three different Cambrian formations in the Great Basin of the western US, corresponding to the west coast of Laurentia (listed here in chronologic order from oldest to most recent): (1) the Pioche Shale of the Chief Range, Lincoln County, southeastern Nevada; (2) the Spence Shale Member (Langston Formation) of the Wellsville Mountains, Box Elder County, northern Utah; and (3) the Marjum Formation of the House Range, Millard County, western Utah. A survey of BST preservation by Gaines et al. (2008) included specimens from each of these localities, thus data are available in the published literature for comparison with that reported here.

Pioche Formation, Chief Range

The Pioche Formation, Nevada, USA, is the oldest BST-fossil bearing unit in the Great Basin region (Delamaran; broadly equivalent to the Series 2–Series 3/Stage 4–Stage 5 boundary) (Brett et al. 2009). Encompassing the *Olenellus* and *Eokochaspis* trilobite zones, the Pioche predates the succession of the House Range Embayment (Lieberman 2003). The Combined Metals Member is mostly limestone but contains some BST fossils in the shale interbeds. The overlying Comet Shale Member is mostly fissile shale, but contains some ribbon limestones (Sundberg and McCollum 2000). Preservationally, the fossils of the Pioche appear to be distinctive, with fluctuating environmental conditions and/or weathering suggested as possibilities for their uniqueness (Lieberman 2003; Moore and Lieberman 2009). One unusual property of the BST fossils of the Pioche Formation is the occasional association of fossils with monazite, a rare-earth-element-bearing phosphate mineral (Moore and Lieberman 2009).

Spence Shale Member, Langston Formation, Wellsville Mountains

In the Spence Shale Member, vermiform fossils are located in a blue-gray micaceous shale (Conway Morris and Robison 1986). The Spence Shale was deposited to the north of the House Range Embayment, in present day Utah and Idaho, USA, in a detrital belt distal to a carbonate belt, and occurs within the *Oryctocephalus indicus/Peronopsis bonner-ensis* trilobite zones (Series 3/Stage 5)—extending slightly geologically older than the Wheeler Formation of the House Range, western Utah (Garson et al. 2012). The Miners Hollow locality of the Spence Shale is more distal than the Antimony Canyon locality and likely had highly variable bottom-water redox conditions (Garson et al. 2012). Fossil priapulids found here are thought to be allochthonous because none of the local trace fossils match priapulid origins (Conway Morris and Robison 1986), and further because BST fossils only occur on bedding planes devoid of burrows. They and other soft-bodied organisms likely washed in with storm turbidity currents (Gaines and Droser 2010).

Table 1.—Specimen details. Information provided includes KUMIP catalog numbers, formation, collection locality, and cataloged identification, all of which were assessed from KUMIP specimen database: http://collections.biodiversity.ku.edu/KUInvertPaleo/). Preservational chemistry reported from analyses conducted here; figure references refer to optical photomicrographs shown here. Pioche Formation specimens were collected at locality 4 of Palmer (1998, fig. 1). Langston Formation (Spence Shale Member) specimens were collected at Miners Hollow (see also localities CF-1 and CF-3 of Sumrall and Sprinkle 1999; Briggs et al. 2008) and Antimony Canyon (locality 781 of Conway Morris and Robison 1986) localities. Marjum Formation specimens were collected at Red Wash (see also locality 716 of Robison and Richards 1981; Briggs et al. 2008) and Sponge Gully (locality 347 of Conway Morris and Robison 1986) localities.

Sample	Formation	Locality	Preservation	KUMIP cataloged identification	Figure reference
293598-P	Pioche	Combined Metals, Ruin Wash, Chief Range	Pyrite association, with euhedral pyrite filling	Ichnofossil	Fig. 2F
293608-Р	Pioche	Combined Metals, Ruin Wash, Chief Range	Pyrite association, with euhedral pyrite filling	Annelida?	Fig. 2H
293611-Р	Pioche	Combined Metals, Ruin Wash, Chief Range	Aluminosilicified, some Fe and Mn oxides	Ichnofossil	Fig. 4A
298531-Р	Pioche	Comet Shale, Ruin Wash, Chief Range	Kerogenized, pyrite-associated surficial features	Ottoia sp.	Fig. 1D
314107-L	Langston	Spence Mbr., Miners Hollow, Wellsville Mts.	Phosphatized, ropy texture	Animalia, unknown	Fig. 5A
314111-L	Langston	Spence Mbr., Miners Hollow, Wellsville Mts.	Kerogenization, pyrite-association, aluminosilicification, bladed barite	Annelida?	Fig. 5C
314112-L	Langston	Spence Mbr., Miners Hollow, Wellsville Mts.	Pyrite-associated outline, annulations	Ichnofossil, Planolites?	Fig. 4F
314114-L	Langston	Spence Mbr., Antimony Canyon, Wellsville Mts.	Pyrite and monazite associations	Animalia, unknown	Fig. 5E
314159-L	Langston	Spence Mbr., Miners Hollow, Wellsville Mts.	Pyrite-association, intermittent gut pyrite filling	Animalia, unknown	Fig. 3A
314186-L	Langston	Spence Mbr., Miners Hollow, Wellsville Mts.	Kerogenization, pyrite-association, aluminosilicification, monazite, calcite	Animalia, unknown	Fig. 6A
314191-L	Langston	Spence Mbr., Miners Hollow, Wellsville Mts.	Pyrite and barite association	Animalia, unknown	Fig. 5I
314202-L	Langston	Spence Mbr., Miners Hollow, Wellsville Mts.	Pyrite-associated outline and surficial features, pyrite-associated gut	Ichnofossil	Fig. 2D
314215-L	Langston	Spence Mbr., Wellsville Mts.	Intermittent pyrite and barite	Annelida?	Fig. 3E
377069-L	Langston	Spence Mbr., Miners Hollow, Wellsville Mts.	Pyrite-associated outline and surficial features, intermittent gut encrustation	Ichnofossil	Fig. 2A
204770-M	Marjum	Sponge Gully, Millard County, House Range	Thinly kerogenized, thickly kerogenized surficial features	Ottoia prolifica	Fig. 1A
314096-M	Marjum	Red Wash, Millard County, House Range	Thinly kerogenized, some pyrite, barite	Ottoia prolifica	Fig. 1F

Marjum Formation, House Range

The House Range suite is a paleontologically and sedimentologically well-studied Cambrian (Series 3-Furongian) succession of deep-water facies deposited in the House Range Embayment (Rees 1986). The House Range includes the fossil-bearing units of (from oldest to most recent) the Swasey Limestone, Wheeler Shale, Marjum Formation, and Weeks Formation (Robison 1964). Generally, these units are a clastic-carbonate mix, with carbonates deposited during local interruptions of clastic sediment supply (Elrick and Snider 2002), for example, during transgressions (Brett et al. 2009). Clastic lithologies dominate, predominantly shales that appear to have been deposited by turbidity currents (Elrick and Snider 2002). Previous, fine-scale ichnological and sedimentological investigation of the Wheeler and Marjum Formations suggests deposition under broadly dysoxic-to-anoxic conditions (Gaines and Droser 2010), although V and Ni redox proxies indicate oxic bottom waters throughout the Wheeler (as well as the above described Spence) Shale (Kloss et al. 2015). The Swasey Limestone corresponds to the Bathyuriscus-Elrathina trilobite zone of Stage 5 (Series 3), which is contemporaneous with the Burgess Shale; the Wheeler Shale and Marjum Formation fall within the Bolaspidella zone of the Drumian-Guzhangian Stages (Series 3); and the Weeks Formation corresponds to the Cedaria zone of the Paibian Stage (Furongian Series) (Robison 1964). BST fossils

from the Marjum Formation are hosted in a blue-gray, finely laminated, calcareous shale that weathers to a yellowish brown (e.g., Robison and Richards 1981; Conway Morris and Robison 1986, 1988)

METHODS

Material

Sixteen specimens of vermiform fossils from the sedimentary deposits of the Great Basin region, accessed from the University of Kansas Biodiversity Institute (KUMIP) collections, were targeted for analyses. These include four specimens from the Combined Metals and Comet Shale Members of the Pioche Formation, ten specimens from the Spence Shale Member of the Langston Formation, and two specimens from the Marjum Formation (see list in Table 1). All KUMIP catalog numbers, when referred to later, will have -P, -L, or -M appended to indicate Pioche, Langston, and Marjum Formations, respectively. Of the analyzed specimens, three belong to the priapulid genus *Ottoia*, two of which are classified at the species level (*O. prolifica*). The other specimens bear few distinguishing morphological characteristics and have tentative assignments in the KUMIP database ranging from annelids and unknown animals to ichnofossils. These specimens, although broadly united as vermiform (worm-like or worm-shaped) in morphology, were not chosen by their

quality of preservation; instead, they were chosen by their appearance of representing a diversity of preservational styles within the spectrum of BST preservation.

Imaging and Spectroscopy

Optical photographs of all specimens were taken with a Nikon D600 digital SLR camera affixed to a Kaiser dual high-frequency fluorescent copystand; micrographs were taken with a boom-mounted Nikon SMZ1500 binocular microscope with attached Nikon DS-Ri1 digital camera. Electron microscopic analyses were conducted with a FEI Quanta 600F (environmental) scanning electron microscope (SEM) with an integrated Thermo Scientific LN2-cooled SiLi energy dispersive X-ray spectrometer (EDS) and a Bruker Quantax 200 silicon drift EDS (installed as a replacement of the SiLi spectrometer) at the University of Missouri Electron Microscopy Core Facility. Electron microscopic imaging constituted imaging of both secondary electrons (SE) using an Everhart-Thornley detector and backscattered electrons (BSE) using a solid-state 4quadrant detector. As the specimens are from museum collections, no destructive preparation techniques were employed and SEM-based analyses were conducted on the native specimens in low vacuum. SEM operating conditions (accelerating voltage, spot size, working distance, etc.) varied between specimens according to optimal quality of data collection.

Statistical Methods

To assess potential differences in fossil-associated clays and those of the host rock matrix, semi-quantitative compositional data were collected using EDS point analyses (n = 319; $n_{\text{matrix}} = 128$, $n_{\text{fossil}} = 175$, $n_{\text{unresolved}} =$ 16). Individual points selected for compositional identification were chosen based on the textures characteristic of clay minerals, as determined by SE imaging. Because many of the anticipated differences in chemistry were simple cation substitutions, spectra were quantified to atomic percentage rather than weight percentage. The compositional data were first compared qualitatively within individual specimens, and, second, subjected to a discriminant analysis in order to identify compositional differences between each of the fossils and their respective host rocks. Only 15 of 16 specimens were included in the discriminant analysis; KUMIP 314215-L was excluded because the fossil boundary was difficult to ascertain in BSE imaging, and thus in positioning of EDS point analyses $(n_{unresolved} = 16)$. For between-specimen comparability, EDS point analyses included in the discriminant analysis were conducted with a beam accelerating voltage of 20 keV (all data reposited in online Supplemental File). Accounting for more than 99% of the total specimen compositions, the eight most abundant elements—oxygen, carbon, silicon, aluminum, iron, potassium, calcium, and magnesium-were included in the discriminant function. The compositional values were arcsine transformed (arcsine of the square root) to prevent common majority elements like oxygen from dominating the variation. Original observations were blindly recategorized as fossil or rock a posteriori based upon the resulting discriminant function in order to test its reliability. The equality of mean discriminant scores for each group (fossil/rock) was tested using Hotelling's T^2 -test. To account for differences in host rock compositions, we subtracted the mean discriminant score for each host rock from the individual fossil discriminant scores. The resulting values were then compared to determine whether there were consistencies in the taphonomic processes influencing the clay mineralogies associated with different fossils. PAST 2.17c was used for all statistical analyses in this study

As many of the specimens used in this study are compression-type fossils, it was additionally important to assess compositional differences with increasing interaction volume depths (see SEM Analytical Consid-

erations section in Discussion, and also methods of Pang et al. 2013; Muscente and Xiao 2015b). Specimen KUMIP 204770-M was subjected to such an assessment, with four separate points examined via EDS with three accelerating voltages (5 keV, 10 keV, and 20 keV). This test was additionally supplemented with Monte Carlo simulations, conducted using the NIST DTSA-II software package.

RESULTS

While each specimen examined in this study shows some taphonomic variation on the general BST preservational theme, the majority are either preserved: (1) as a kerogenized carbon film, or (2) with an abundance of associated pyrite framboids. Many of the pyrite framboids have been diagenetically oxidized or weathered to iron oxides but retain framboidal crystal habits. For convenience, iron oxides inferred to have been pyrite from crystal habit are collectively referred to as pyrite. In addition, all of the analyzed specimens have recognizable clays associated with the fossil materials, which allowed for comparison of fossil clays and host rock clays by the discriminant analysis described above, although only one specimen can be considered preserved predominantly via aluminosilicification. These variations on the BST theme are described by dominant mineralization or preservational style below.

Predominantly Kerogenized Specimens

Three of the specimens are preserved mainly via kerogenization: KUMIP 298531-P from the Pioche Formation (Lieberman 2003), and KUMIP 204770-M (Conway Morris and Robison 1986) and 314096-M, both from the Marjum Formation (Fig. 1). These three, the only specimens to exhibit adequate detail to allow classification, all belong to the priapulid genus *Ottoia*. Optically, kerogenization of these specimens appears to capture fine morphological details, such as annulations and gut tracts (Fig. 1A, 1D, 1F), apparent as areas of darker coloration. While these specimens of *Ottoia* appear to have similar preservation when viewed optically, electron microscopy reveals their differences, as described below.

In SEM examination, specimen KUMIP 204770-M (Fig. 1A) displays annulations (Fig. 1B) and a gut tract comprised of discernable patches of kerogen. These patches show cracked textures reminiscent of sedimentary desiccation features (Fig. 1C). The areas with kerogen patches are discontinuous, and no carbon film is visible between them in BSE imaging, although the optical appearance and coloration of this fossil gives the impression that such a film should be present. EDS analysis with multiple accelerating voltages (Table 2) also does not show evidence of a thin carbon film in the interannular space. KUMIP 204770-M is very flat, only showing significant topography on the kerogen patches. Aside from the carbon patches, the compositions of the host rock and fossil seem to be very similar, but the clay texture is notably different. Specifically, the fossil-associated clays exhibit a smoother appearance and preferred orientation (Fig 1C, right) as compared to those of the host rock matrix (Fig. 1C, left).

KUMIP 298531-P (Fig. 1D) exhibits a similar mode of preservation to KUMIP 204770-M. KUMIP 298531-P exhibits annulations as topographic features as well as kerogeneous patches, which are much more distinct than in KUMIP 204770-M. Framboidal pyrite is also present in KUMIP 298531-P, occurring in thin linear features following the center of the kerogeneous patches (Fig. 1E).

KUMIP 314096-M (Fig. 1F), in addition to kerogen patches, bears traces of annuli, which, upon SEM inspection, are preserved as bands of different clay textures (Fig. 1G) as opposed to kerogeneous features like KUMIP 204770-M and 298531-P. Unlike KUMIP 204770-M, the majority of KUMIP 314096-M does not exhibit a smooth clay surface. The annulations themselves are considerably rougher, and appear darker in backscattered electron imaging. EDS analysis shows that the average

604

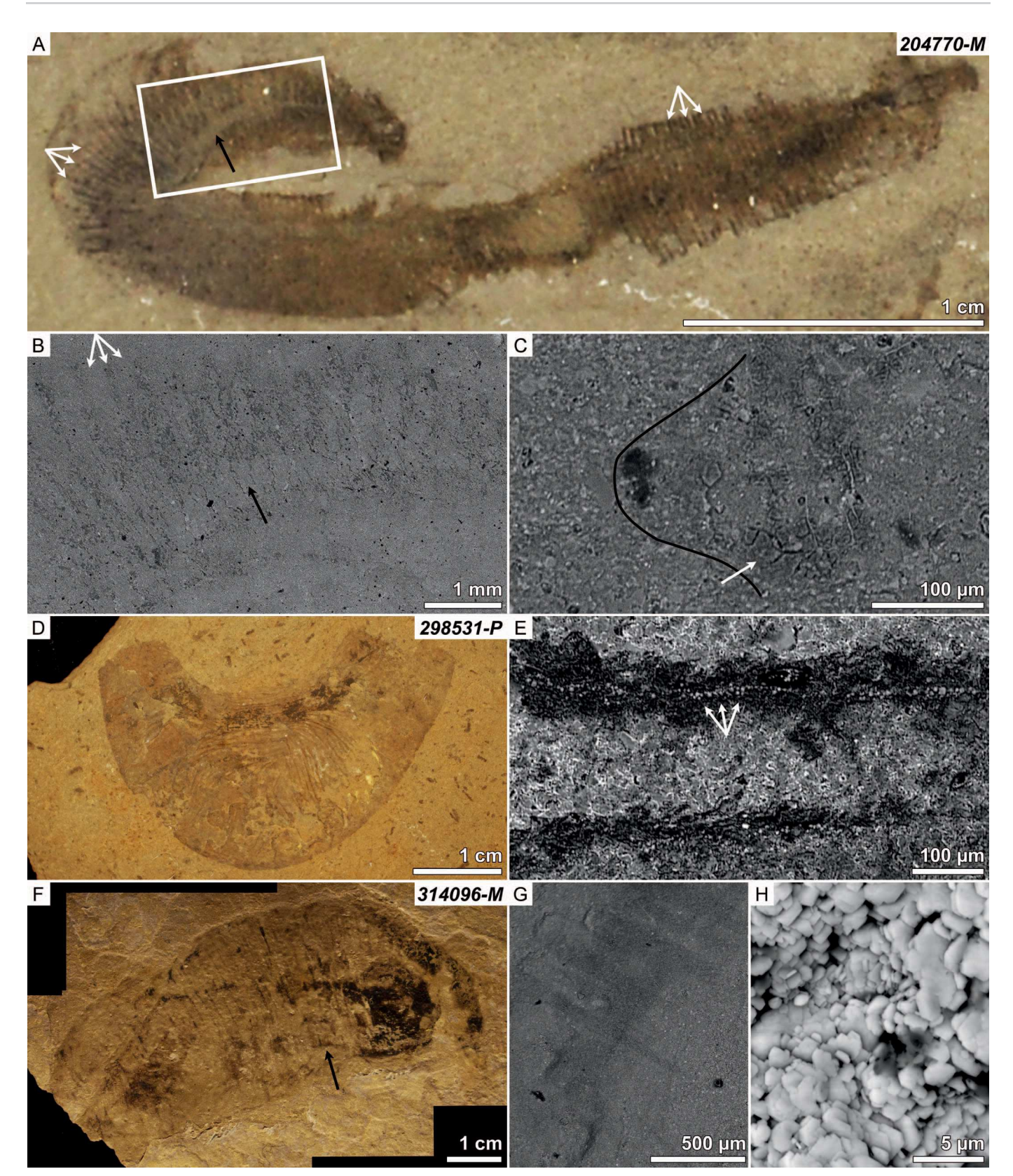


Fig. 1.—Predominantly kerogenized specimens, all of which belong to the genus *Ottoia*. (A–C) are KUMIP 204770-M; (D–E) are KUMIP 298531-P; and F–H are KUMIP 314096-M. **A)** Optical photomicrograph of 204770-M. **B)** BSE image [from rectangle area in (A)] of annulations (white arrows) and gut (black arrow). **C)** Kerogen patches and clay textures inside vs. outside of fossil material. Note cracked texture of kerogen patches due to volumetric reduction (white arrow), and smoother, finer-grained nature of clays associated with fossil material (right) as compared to those of the host rock (left). Black line corresponds to body wall. **D)** Optical photomicrograph of 298531-P. **E)** Thin line of framboidal pyrite (white arrows) within bands of kerogen (darker surrounding material). **F)** Optical photomicrograph of 314096-M. **G)** bands of different clay textures preserving annuli [from black arrow region in (F)], note differing grayscale. **F)** Detail of bladed barite patches.

Table 2.—EDS data acquired at different accelerating voltages (V_0), in kiloelectron volts (keV). Points were positioned both on and near a kerogen patch associated with an annulation and interannular space, respectively, in KUMIP 204770-M. Increasing accelerating voltages yield signal from greater depths beneath the specimen surface.

Point	V_0 (keV)	C	O	Mg	Al	Si	S	K	Ca	Fe
Kerogen patch pt 1	5	51.14	30.14	0.69	6.76	11.26	0	0	0	0
	10	43.26	42.41	1.55	3.63	4.7	0	0.55	2.74	1.15
	20	21.43	52.43	1.52	6.54	12.16	0.48	1.57	2.23	1.65
Kerogen patch pt 2	5	49.4	39.22	1.33	3.86	6.2	0	0	0	0
	10	15.26	52.72	1.81	10.16	15.4	0	2	1.42	1.23
	20	8.75	61.03	1.07	8.24	16.52	0	1.84	0.91	1.64
Interannuli pt 1	5	11.44	60.55	4.9	10.59	12.52	0	0	0	0
	10	9.18	61.81	5.84	9.58	9.94	0	0	0	3.65
	20	28.79	49.42	0.62	4.63	14.28	0	1.15	0.69	0.43
Interannuli pt 2	5	12.3	44.81	1.7	9.5	31.69	0	0	0	0
•	10	24.27	52.28	0.53	4.35	11.79	1.98	1.05	3.04	0.71
	20	31.88	28.56	0.53	6.83	25.9	0.91	2.66	1.65	1.07

carbon atomic percentage is five percent higher on the rough, dark material (26.8%) than the smooth, light material (21.8%); however, the standard deviation of carbon content is high in the light material (9.0, as opposed to 4.2 on the rough, dark material), and thus the significance of this distinction is less certain. Moreover, the standard deviation of every detected element is higher between the annuli than on the annuli, potentially a result of topographic roughness impacting EDS signal (e.g., see discussions in Orr et al. 2009; Orr and Kearns 2011). Even considering the high variation of composition in the space between the annulations, the annuli themselves are clearly higher in iron and magnesium. KUMIP 314096-M also contains large (> 1 mm) patches of bladed barite encrusting the surface of part and counterpart (Fig. 1H).

Predominantly Pyritized Specimens

Most commonly in the examined material, pyritization occurs as elevated concentrations of pyrite contiguous to fossil boundaries/edges or directly associated with specific morphological features (Fig. 2). KUMIP 377069-L (Fig. 2A) and 314202-L (Fig. 2D), both of which are designated as ichnofossils, display annular features, represented by diffuse, noncontinuous bands of localized framboidal pyrite (e.g., Fig. 2B). In some pyrite framboids, individual grains contain objects that are too small to identify their composition (Fig. 2E). These objects, averaging 240 nm in diameter, appear darker than pyrite in backscattered electron images. KUMIP 293598-P (Fig. 2F), also catalogued as an ichnofossil, exhibits an unusual style of pyritization where partly-intergrowing pyrite euhedra fill sections of the fossil, though much interstitial space remains (Fig. 2G). KUMIP 293608-P (Fig. 2H), a presumed annelid, has similar euhedra, though less densely packed. The pyrite crystallites in some specimens appear to be broken open, exposing material on which the pyrite may have nucleated. For instance, some euhedral pyrite in KUMIP 293608-P seems to have overgrown small clay booklets (Fig. 2I).

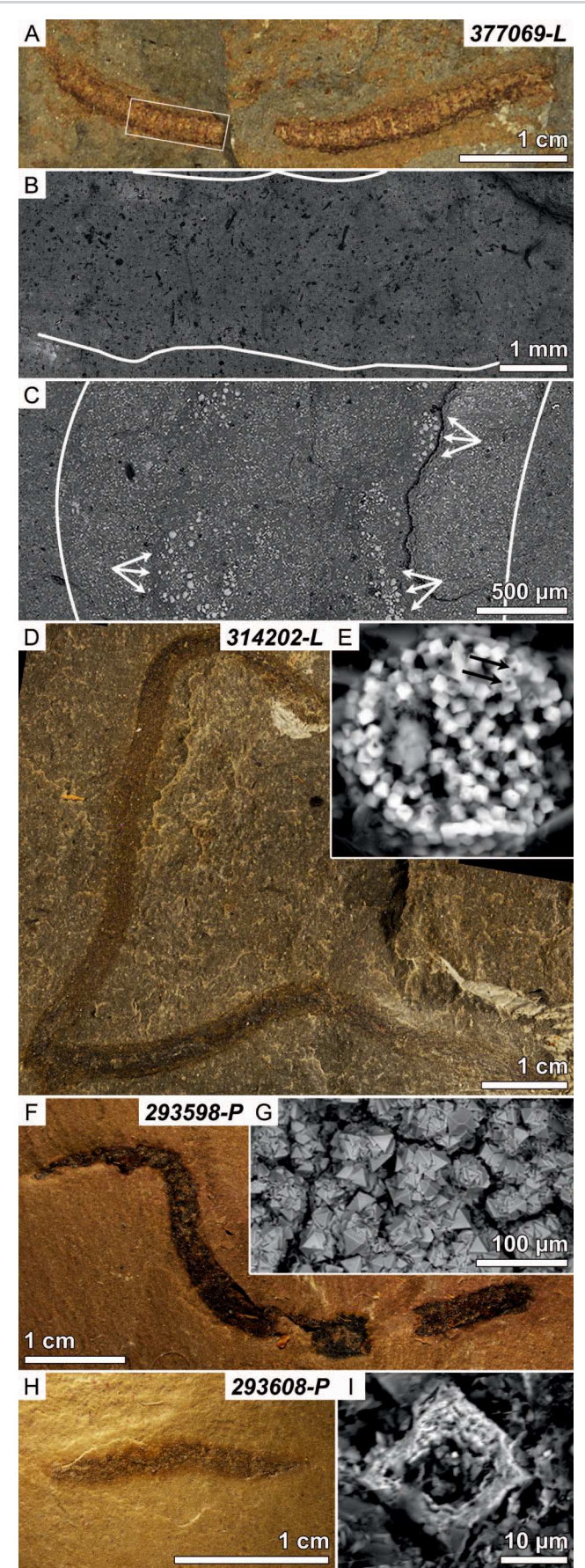
Some specimens contain what appear to be pyrite-associated or more pervasively pyritized gut tracts (examples in Figs. 2, 3). Gut tracts are identified where there is a transverse zone of different characteristics, either observationally or compositionally, that is medially located. Usually, the pyritized portion of the gut does not extend through the length of the entire specimen, but is instead an intermittent feature. The pyrite-associated gut tracts manifest as elevated concentrations of pyrite within the gut region and with pyrite concentrated along the border of the gut presenting as a defined outline. Other specimens preserve the gut tract as a completely pyrite-infilled (pervasively pyritized) three-dimensional feature. These features can typically be ascertained either optically, as in specimens KUMIP 314159-L (Fig. 3A; an unknown animal), 314202-L (Fig. 2D),

and 314215-L (Fig. 3E; a suspected annelid), or by BSE imaging, as in KUMIP 377069-L (Fig. 2B, 2C).

The most extreme case of gut tract pyritization is KUMIP 314159-L, in which the pyrite exhibits large, euhedral and acicular crystals (Fig. 3B). This pyrite encrusts large (up to 30 µm wide and 1-2 µm thick) tabular clay minerals (Fig. 3C), which, unlike clays occurring elsewhere in the fossil or host rock, are almost completely devoid of carbon and calcium. These clay minerals are sometimes enveloped by a thin crust of pyrite, followed by a layer of pyrite with a botryoidal morphology (Fig. 3D). Due to the three-dimensional nature of pyritization in their innermost zone, KUMIP 314159-L is considered to have a pyrite-infilled gut tract. On the other end of the spectrum, KUMIP 377069-L does not optically appear to possess a preserved gut as it shows little apparent medial differentiation. However, upon BSE inspection, this specimen shows intermittent pyrite framboids, in some areas arranged in two nearly parallel bands (Fig. 2B, 2C), around the border of a presumed gut and body wall. KUMIP 293608-P and 314215-L represent indeterminate cases. KUMIP 314215-L optically appears to have a central, defined feature different from the rest of the specimen (Fig. 3E). While sections of this central feature are visible with microanalysis, the surrounding body is not visible. KUMIP 314215-L is also unusual in that, instead of pyrite association (or iron oxide pseudomorphs thereof) with the presumed gut, this central feature is replicated in barite (Fig. 3E, 3F). KUMIP 293608-P is less determinate still, and appears optically undifferentiated and uniformly preserved. This uniform preservation, however, shows resemblances, on the whole, to the pyrite-related preservation of the differentiated guts from the other specimens, with concentrations of pyrite along the outermost edges of the fossil.

Predominantly Clay-Associated Specimen

Only one of the examined specimens appears to be preserved mainly in aluminosilicate replication or templating. Optically, KUMIP 293611-P (interpreted as an ichnofossil) is a vivid red in color (Fig. 4A), which distinguishes it from the dull brown, gray, and orange colorations of the other fossils. The fossil exhibits two zones: an interior portion with brighter coloration, and a wider bordering area that is duller. The surface of KUMIP 293611-P has considerably higher BSE signal than the clays of the host rock (Fig. 4B), indicating higher average atomic number, yet has similar mineral textures observed on other specimens in this study. The interior portion of the fossil shows an elevated BSE signal relative to both the outer zone of the fossil and the host rock. The fossil, and especially its interior zone, shows elevated concentrations of carbon and iron, likely corresponding to interstitial carbon and iron-bearing clays. At least



cursorily, KUMIP 314112-L (Fig. 4F) appears similar to KUMIP 293611-P, although with different coloration. This fossil shows comparable inner versus outer zonation, but preservation much more comparable to KUMIP 377069-L with pyrite framboids along the fossil boundary and perhaps annular features.

In addition to having a somewhat unique taphonomic mode for vermiform fossils in this sample set, KUMIP 293611-P has additional unusual properties. On the surface of the fossil, there are numerous carbonrich objects, which appear to be deflated spherules of organic carbon, $\sim 100~\mu m$ in diameter (Fig. 4C). Morphologically, these objects resemble simple, spherical acritarchs; EDS analysis shows that they are rich in carbon (70.3%) and nitrogen (6.8%), with additional aluminum, silicon, oxygen, and iron components likely derived from X-ray signal generated by the host rock beneath these objects. Another unusual feature of KUMIP 293611-P is a pattern of iron and manganese oxide mineralization that occurs on one end of the fossil (Fig. 4D). EDS elemental maps show alternating layers of iron and manganese extending outward from one end of the fossil, and ending in branching iron and manganese oxide structures (Fig. 4E).

Calcium-Associated and Phosphatized Specimens

Seven specimens, including KUMIP 314159-L, 293598-P, 293608-P, 293611-P, 314107-L (Fig. 5A; an unknown animal), 314111-L (Fig. 5C; a suspected annelid), and 314186-L (Fig. 6A; an unknown animal) show elevated concentrations of calcium with the fossils. One specimen, KUMIP 314186-L, is associated with a calcium carbonate crust on part of the fossil (Fig. 6F). Another specimen, KUMIP 314107-L, is almost entirely composed of calcium phosphate. This 7-mm wide fossil is black in color, with a ropy texture, and between the "ropes" of calcium phosphate are pockets of clay minerals that vary in composition between individual pockets (Fig. 5B). It is thus likely that the calcium phosphate beneath the clays contributes to the characteristic X-rays at those points, consistent with there being a noticeable phosphorus signal in the same points.

Taphonomic Oddities

KUMIP 314114-L (Fig. 5E; an unknown animal) is unique in the combination of minerals present, but otherwise exhibits features and morphologies in common with other specimens in this study. Within the fossil, there is an elevated concentration of framboidal pyrite. Some areas have patches of visible carbonaceous material. The medial section of the fossil, interpreted as the gut tract, contains intermittent zones of monazite crystals that fan out in many directions without any obvious trend. Within these monazite zones, there are occasional pockets of pyrite or oxide psuedomorphs, consisting of large (5–15 μ m) framboids and small (< 5 μ m) octahedra, with a granular texture in-between (Fig. 5G). Other parts of the monazite show granules of calcium-rich minerals and barite. Beyond the zones of monazite, there are smaller needles of randomly oriented monazite (Fig. 5F), some of which show twinning at 90°.

Fig. 2.—Predominantly pyritized specimens. (A–C) are KUMIP 377069-L; (D, E) are KUMIP 314202-L; (F, G) are KUMIP 293598-P; and (H, I) are KUMIP 293608-P. A) Optical photomicrograph of 377069-L. B) Pyrite concentration along the edges of the fossil and diffusely spread over the medial portion, from rectangle area in A (white lines indicate body wall). C) pyrite framboids in parallel bands through medial portion of the fossil [rotated $\sim 90^\circ$ from orientation in (A) or (B)]. Note the size difference in pyrite framboids near the center of the fossil (white arrows), presumed to be along gut wall. White lines indicate body wall as before. D) Optical photomicrograph of 314202-L. E) Nanoscale objects within individual crystals of a pyrite framboid (black arrows; framboid diameter = $\sim 16~\mu m$). F) Optical photomicrograph of 293598-P. G) Intergrowing pyrite euhedra. H) Optical photomicrograph of 293608-L. I) Clay within a pyrite euhedron.

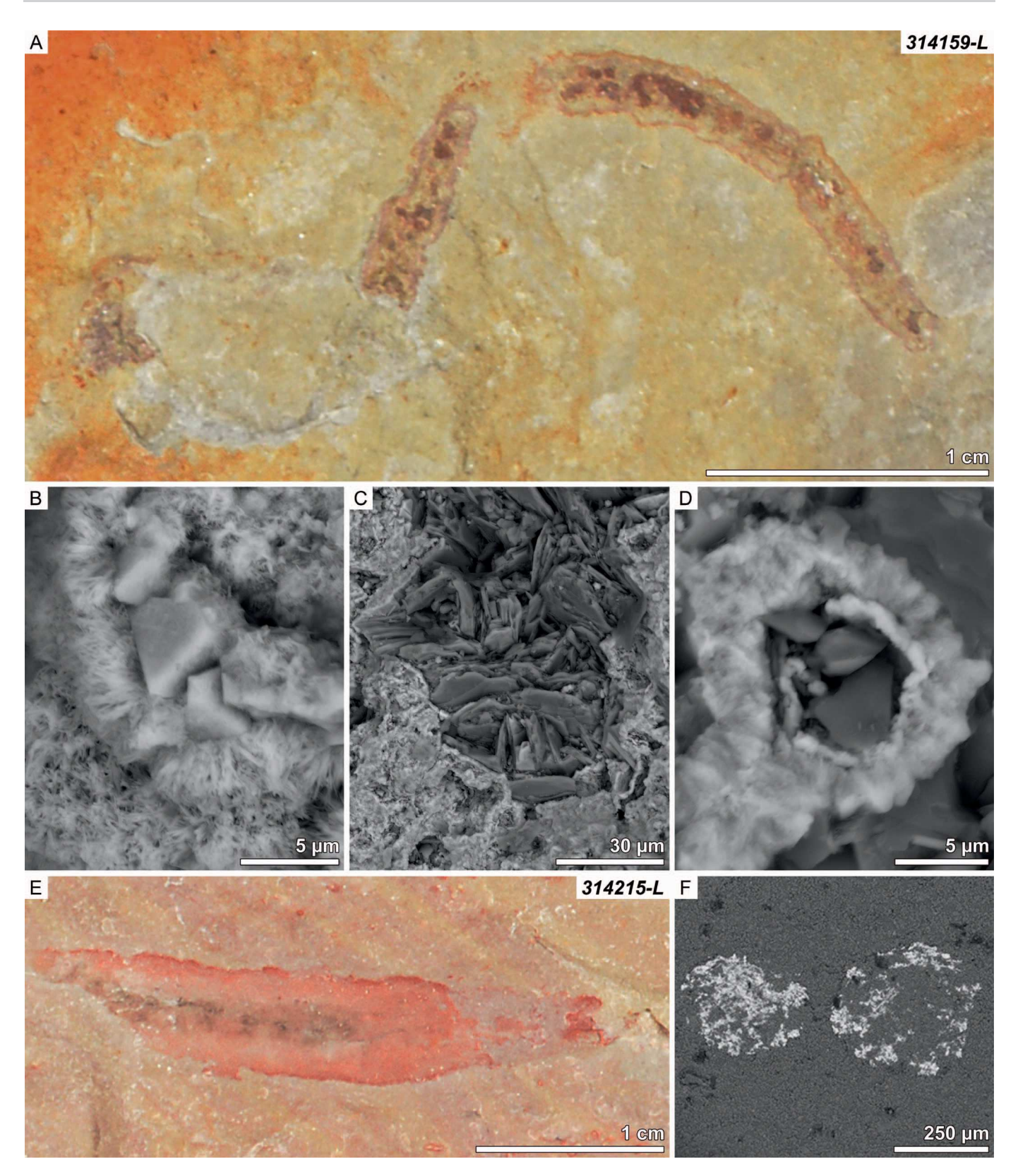


Fig. 3.—Fossils with visible gut tract preservation. (A–D) are KUMIP 314159-L; (E, F) are KUMIP 314215-L. **A)** Optical photomicrograph of 314159-L. **B)** Pyrite euhedra overgrown with acicular pyrite. **C)** Tabular gut clays overgrown with pyrite. **D)** Clays overgrown with pyrite crust, and then larger pyrite with botryoidal morphology; (B–D) are all found in the darker, medial region of 314159-L. **E)** Optical photomicrograph of 314215-L. **F)** Circular barite features in medial portion of 314215-L.

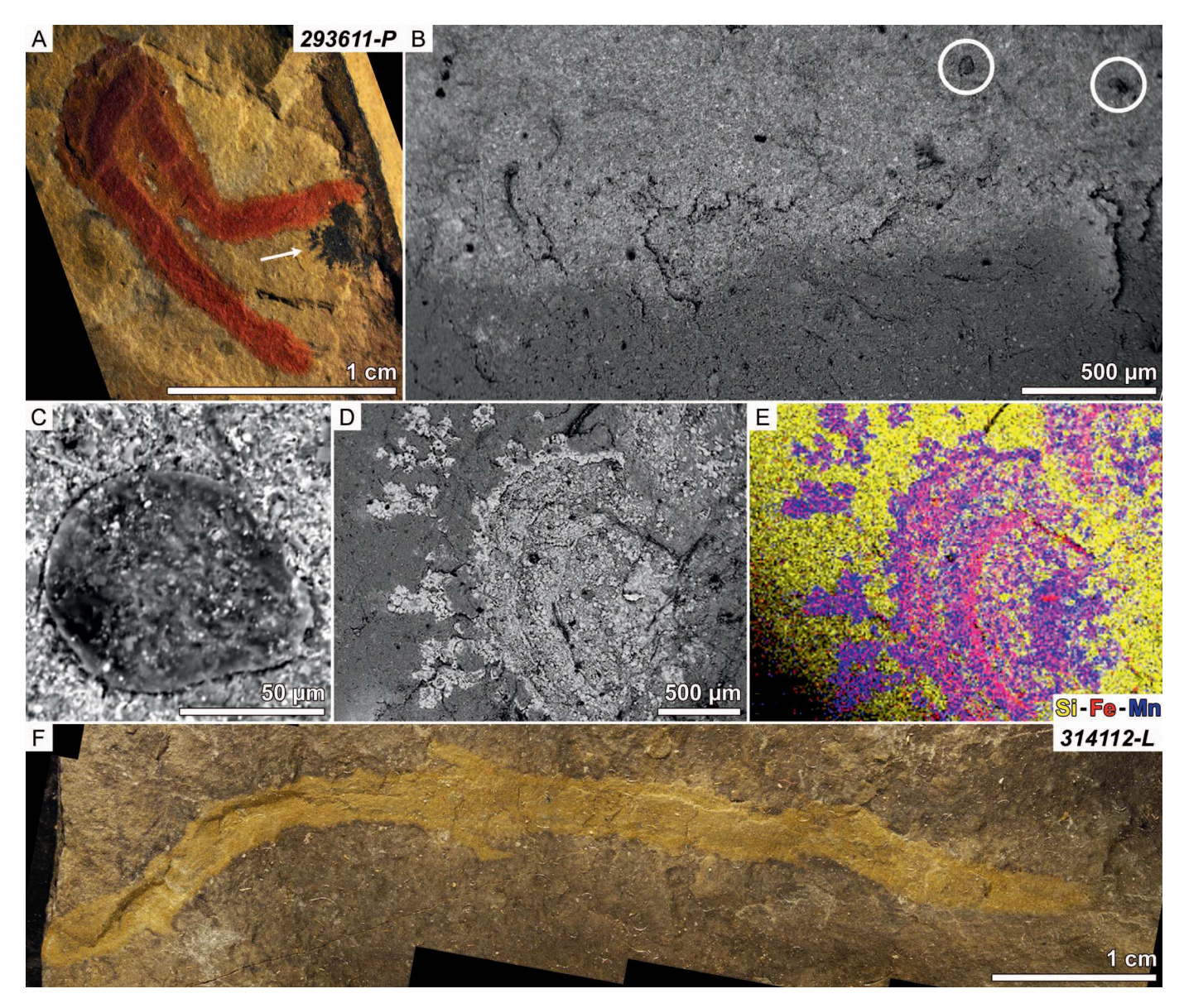


Fig. 4.—Clay association. (A—E) are KUMIP 293611-P; (F) is 314112-L. A) Optical photomicrograph of 293611-P. B) BSE contrast between fossil (bright/high signal, upper) and host rock matrix (dark/low signal, lower), generally corresponding to higher iron concentrations in the fossil; circles indicate carbonaceous objects. C) One of the carbonaceous objects found within the fossil. D) BSE micrograph of iron and manganese oxide banding; arrow in (A). E) EDS elemental map for D. F) Optical photomicrograph of KUMIP 314112-L.

Another unusual feature of KUMIP 314114-L is its gut contents. KUMIP 314114-L contains a medially located phosphatic object, the teardrop shape of which resembles a lingulid brachiopod shell (Fig. 5E, 5H). The object is ~ 2 mm in length and exhibits a pronounced apex. Though the shell appears to be in poor condition, the surface exhibits numerous pores reminiscent of lingulid punctae. The surface also bears elongate rectangular grooves (up to 20 μm in length) that reveal a porous lattice in the subsurface (inset in Fig. 5H). The poor condition of this shell, including the grooves, could be the result of digestive etching, which may indicate that this worm could have been a predator or detritivore of brachiopods. Fractures in the shell contain clay tabulae of much coarser fabric than the host rock. The shell also exhibits a band of carbonaceous material that starts at the tip of the posterior and extends nearly across the entire shell towards the anterior.

608

KUMIP 314186-L (Fig. 6) contains two zones that run along the entirety of the specimen's length, which may represent the gut tract and body. The gut tract is much more readily visible in BSE images than the body. The gut tract has higher BSE signal than the host rock, whereas the body exhibits a lower BSE signal. Compositional analysis via EDS shows that the inferred gut tract contains lower carbon content (7.2 at. %; n = 8) than the either the body portion (14.1 at. %; n = 11) or the host rock (13.9 at. %; n = 5). In secondary imaging, this difference is more visible as charge contrast, with the gut tract exhibiting more contrast and the body exhibiting less contrast than the host rock. Monazite is also present in KUMIP 314186-L, including needles and stellate structures (Fig. 6C). Although monazite occurs in both the gut region and the body region, the majority is concentrated along the boundary between the gut and the body. Within the gut, the monazite is surrounded by coarse (up to 41 µm-wide) clay tabulae

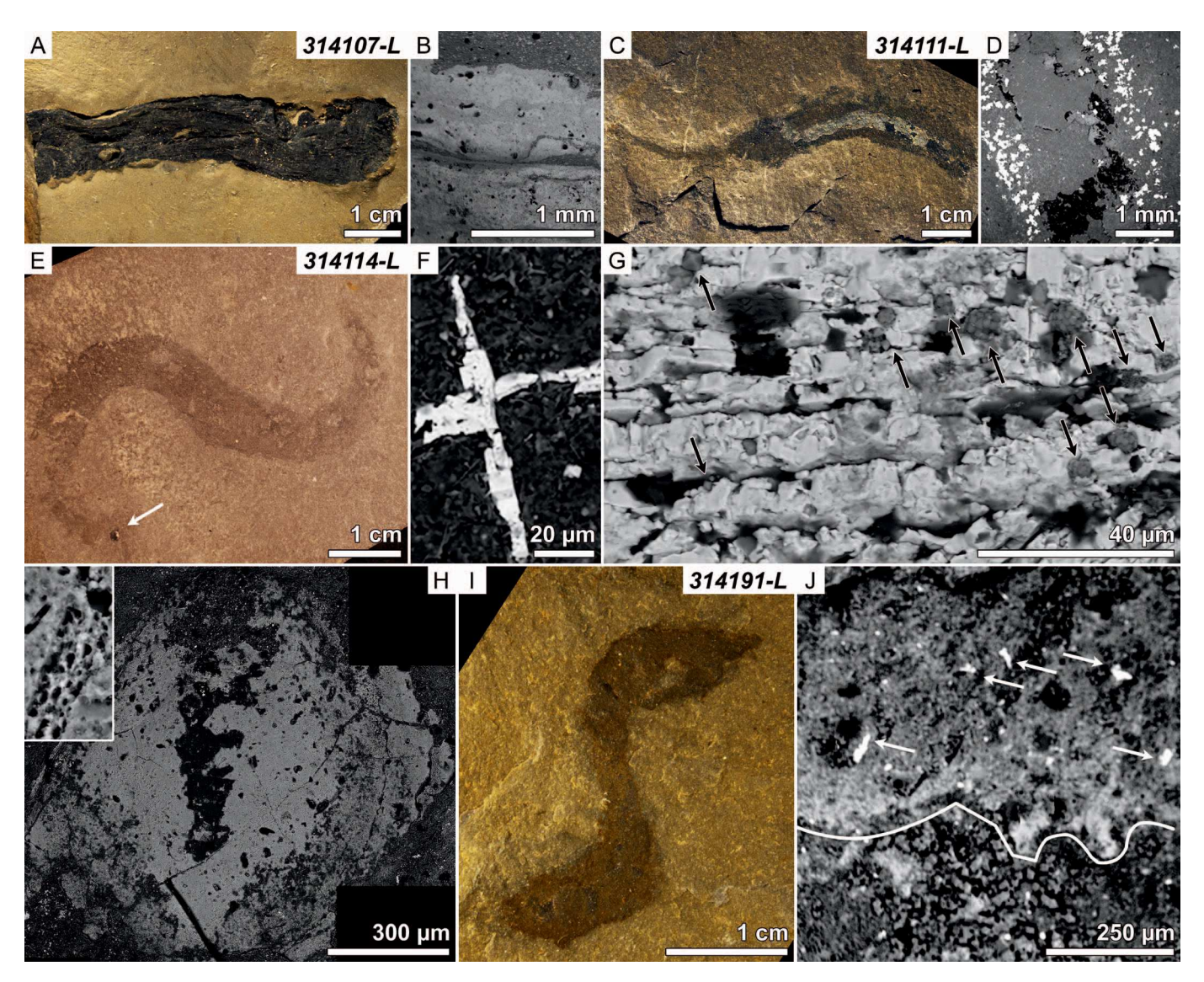


Fig. 5.—Taphonomic oddities. (A, B) are KUMIP 314107-L; (C, D) are KUMIP 314111-L; (E–H) are KUMIP 314114-L; (I, J) are KUMIP 314191-L. A) Optical photomicrograph of 314107-L. B) BSE image of carbon film (black) and barite (white) within medial portion of 314111-L. E) Optical photomicrograph of 314114-L. F) BSE image of monazite, with twinning at 90° . G) BSE image of monazite zone within medial portion of 314114-L, note included pyrite framboids and euhedra (outlined black arrows). H) Possible lingulid valve [presumably gut content, see arrow in (E)], inset in upper left (inset frame width = $12 \mu m$) shows shell microstructure. I) Optical photomicrograph of KUMIP 314191-L. J) BSE image with barite blades (white arrows) and high contrast between fossil and host rock (boundary denoted by white line).

(Fig. 6D), which exhibit higher carbon and lower iron than the other clays in the fossil. In parts of the fossil, a clearly visible carbon film, with embedded framboidal pyrite (Fig. 6E), is present on the gut tract. This carbon film is oxygen-poor, consistent with a mature kerogen. Two sets of fractures run through the carbon film, showing an orientation that does not change even when the fossil bends or twists.

Examination of the part and counterpart of KUMIP 314186-L revealed distinctive vertical relationships among some of the minerals present in the specimen. The upper surface of the specimen was buried underneath a turbidite consisting of small ($\sim 25~\mu m$) grains of calcite, which exhibit normal grading (Fig. 6F). This contrasts greatly with the underlying sediment, which is comprised of calcium-deficient phyllosilicates. The carbonaceous film overlies an intermittent crust of iron-rich clays (Fig. 6G), and, occasionally, calcium carbonate. The calcium carbonate does not

show any crystallographic features, but the iron-clay crust is composed of fine (\sim 40 μm -long, \sim 5 μm -wide) needles oriented normal to the carbon film.

Much like KUMIP 314186-L above, KUMIP 314111-L (Fig. 5C) has a very distinct carbon film with a fracture pattern that seems unrelated to the original morphology of the worm (Fig. 5D), comparable to that observed on KUMIP 314186-L (Fig. 6B). On both sides of this film, there is a coating of clay minerals, which exhibit lower iron content than the host rock. Along the lateral edges of the fossil is a zone of abundant barite $\sim 600~\mu m$ wide (Fig. 5D). At parts, the barite zone appears to overlie the clay crust that overlies the carbon film. This indicates that the barite envelops the fossil. If this fracture surface only exposes material along a thin plane, additional barite could be concealed within the part and counterpart, encircling the specimen.

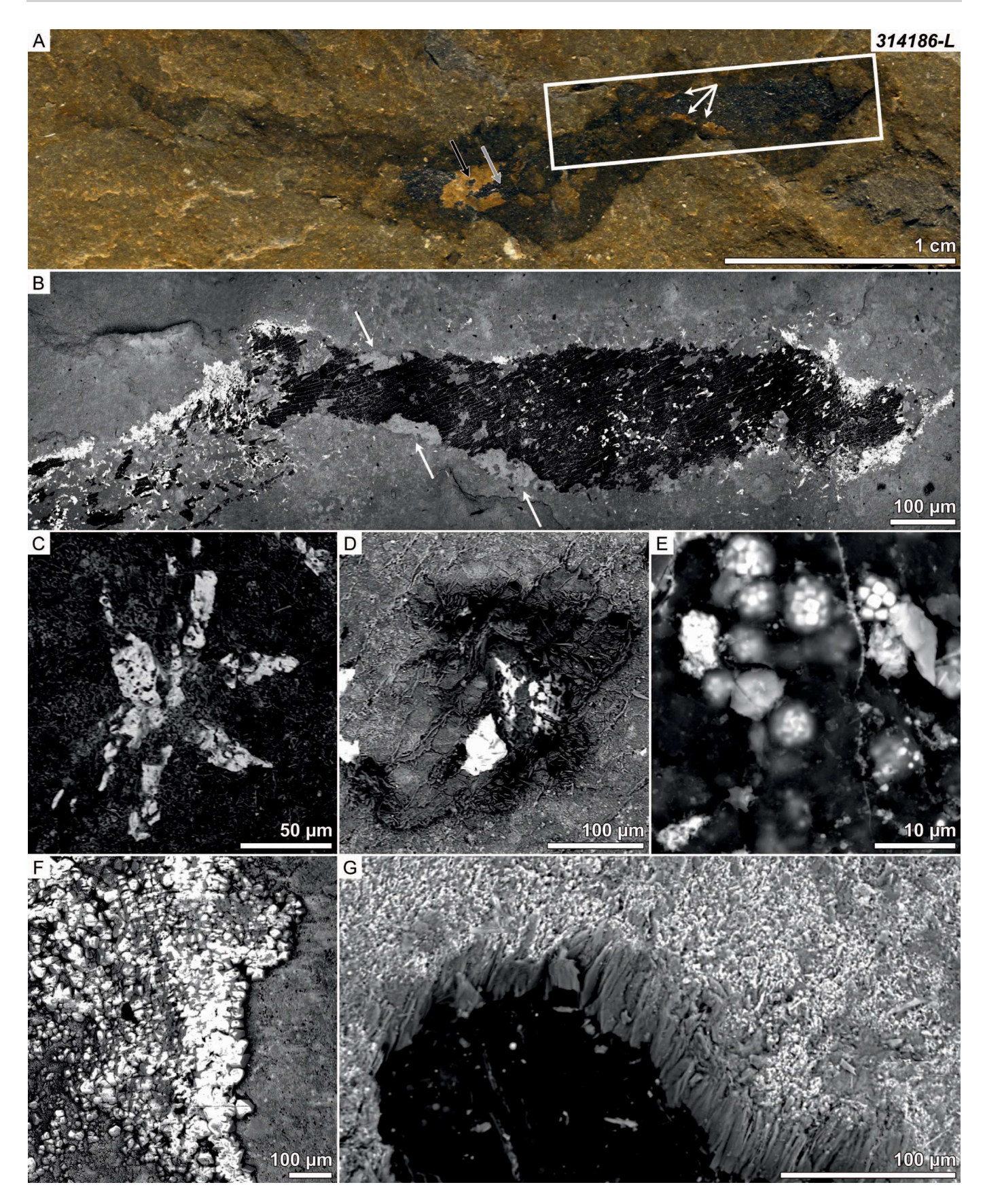


Table 3.—Discriminant scores for points from fossils and their host rocks. Positive $\Delta_{fossil-rock}$ values correspond to more characteristic fossil-like compositions. KUMIP 314111-L was the only specimen to defy this trend.

Sample	Host rock	Fossil	$\Delta_{ m fossil-rock}$
293598-Р	0.4395	0.4829	0.0434
293608-P	0.2145	1.0255	0.8110
293611-Р	-0.2371	0.2219	0.4590
298531-Р	-0.3292	-0.1661	0.1631
314107-L	0.3053	0.6908	0.3855
314111-L	0.0294	-0.1846	-0.2140
314112-L	-0.2992	0.0505	0.3497
314114-L	-0.4454	-0.1126	0.3328
314159-L	-0.1263	0.2527	0.3790
314186-L	0.1447	0.2103	0.0656
314191-L	-0.6437	0.0335	0.6772
314202-L	-0.3862	0.0980	0.4842
377069-L	-0.2450	0.4429	0.6879
204770-M	-0.1720	-0.1437	0.0283
314096-M	-0.0105	0.0657	0.0762

Discriminant Analysis Results

Discriminant analysis was employed to test for general compositional differences between fossils and their host rocks, using compositional data from EDS point analyses (included in online Supplemental File). Categorizing the compositional data by fossils and host rocks yields a discriminant function—an equation that, for any given composition, calculates a discriminant score indicating whether a given composition is host-rock-like (negative) or fossil-like (positive):

$$-8.957*Mg + 6.999*Fe - 6.943*K + 3.494*Si + 2.163*Al \\ + 1.345*Ca - 0.826*O + 0.080*C$$

The discriminant function is largely driven by magnesium (associated with negative discriminant scores) and iron (associated with positive discriminant scores), as indicated by the coefficients for Mg and Fe. In this function, fossil-associated clays had higher discriminant scores than host rock clays (Table 3). Hotelling's T^2 -test showed a significant difference (p = 0.0026) between the two distributions, and 58.42% of points were correctly reclassified. The two distributions largely overlap (Fig. 7A), but the distribution of fossil points is more right-skewed (skewness = 1.66, versus 0.53 for host rock).

Iron and magnesium can readily substitute for one another in clay minerals. To test the importance of iron in this discriminant analysis, the discriminant analysis was repeated without iron, and then repeated without magnesium. The discriminant analysis without iron had a non-significant p-value for Hotelling's T^2 (p = 0.361), and a smaller percentage of correctly reclassified points (55.12%) as compared to the original analysis. The discriminant analysis without magnesium was considerably better than the discriminant analysis without iron, with a significant Hotelling's T^2 p-value (p = 0.0081) and only a marginally smaller percent correctly reclassified (57.76%) as compared to the discriminant analysis with all elements. To control for differences in host rock composition between specimens, the average discriminant score for each specimen's host rock was subtracted from that of each fossil point, yielding a distribution (Fig. 7B) where 59%

of fossil points have a higher discriminant score than their host rock ($t = 5.727, p = 4.406*10^{-8}$). Further, six of the 15 fossil specimens individually showed significantly higher means than their host rock (*Student's t*-test, p < 0.05). With high fossil-associated magnesium and potassium concentrations, KUMIP 314111-L is the only specimen to show a lower discriminant score than its host rock.

DISCUSSION

SEM Analytical Considerations

With the accessibility of advanced analytical instruments like SEMs, these tools have become routinely used in paleobiological investigations. However, they are not without their limitations, and one can easily produce data prone to misinterpretation without careful consideration of operating conditions. Several recent studies have offered cautions and caveats for SEM-based approaches in paleobiological research, many of which have focused on BST or comparable compression-type fossils (Orr et al. 1998; Orr et al. 2002; Orr et al. 2009; Orr and Kearns 2011; Muscente and Xiao 2015b). Further, texts such as that by Goldstein et al. (2003) provide invaluable resources for understanding the principles of SEM microanalyses. With such caveats in mind, we present a brief aside to describe mitigations and considerations taken in the analyses of the specimens presented here.

A primary consideration in SEM analyses is that we are dealing with numerous signals produced during the electron beam-specimen interaction, and that these signals are derived from an interaction volume (e.g., Goldstein et al. 2003; Orr and Kearns 2011). Generally, this volume is teardrop-shaped, extending into the specimen material from the spot of the electron beam impingement on the specimen surface. The signals that are generated during beam interaction have differing depths from which they can be emitted, or differing excitation volumes, proportionate with the energy of the signal. From top to bottom (shallowest to deepest) within the interaction volume, the relevant signals in this study are emitted as follows: secondary electrons for topographic imaging, emitted from approximately the upper 500 Å (0.05 µm); backscattered electrons, emitted from within the uppermost several µm; and characteristic x-rays, the range of which is a substantial fraction of the full electron interaction volume. It is inherently difficult to put numbers on these depths, as the depth of penetration of the beam is related to both beam accelerating voltage and density/atomic number of the material being analyzed. This is especially challenging when dealing with specimens that are heterogeneous with depth, although tests conducted here such as analyses at differing accelerating voltages (Table 2) and Monte Carlo electron trajectory simulations can prove useful for assessing compositional heterogeneity and modeling interaction depths, respectively (Goldstein et al. 2003; Orr et al. 2009; Orr and Kearns 2011; Muscente and Xiao 2015b).

One of the most commonly used signals is that of backscattered electrons. BSE imaging is an effective means of discerning compositional information at a glance, but it is not without its shortcomings. Backscattered electrons are primary beam electrons that have been redirected out of the specimen through (one or more) elastic scattering interactions. These electrons have a higher energy than those emitted during inelastic scattering interactions, or secondary electrons ejected from specimen atoms, and as such yield a signal emanating from deeper within the specimen. As a consequence of the detectability of these interactions

Fig. 6.—Unique features of KUMIP 314186-L. A) Optical photomicrograph, arrows in rectangle indicate clays (brownish in color). B) BSE image of section of presumed gut [rectangle area in (A)] showing relationship of kerogen (black), monazite (white), and clay (gray patches immediately surrounding kerogen, arrows), note the fracture pattern in the carbon film. C) Stellate monazite. D) Clay tabulae and monazite. E) Pyrite framboids enveloped within carbon film [outlined gray arrow in (A)]. F) Calcareous grains on upper fossil surface, grading from coarser to finer grains. G) Iron-rich clay occurring on the underside of the carbon film, note perpendicular orientation [outlined black arrow in (A)].

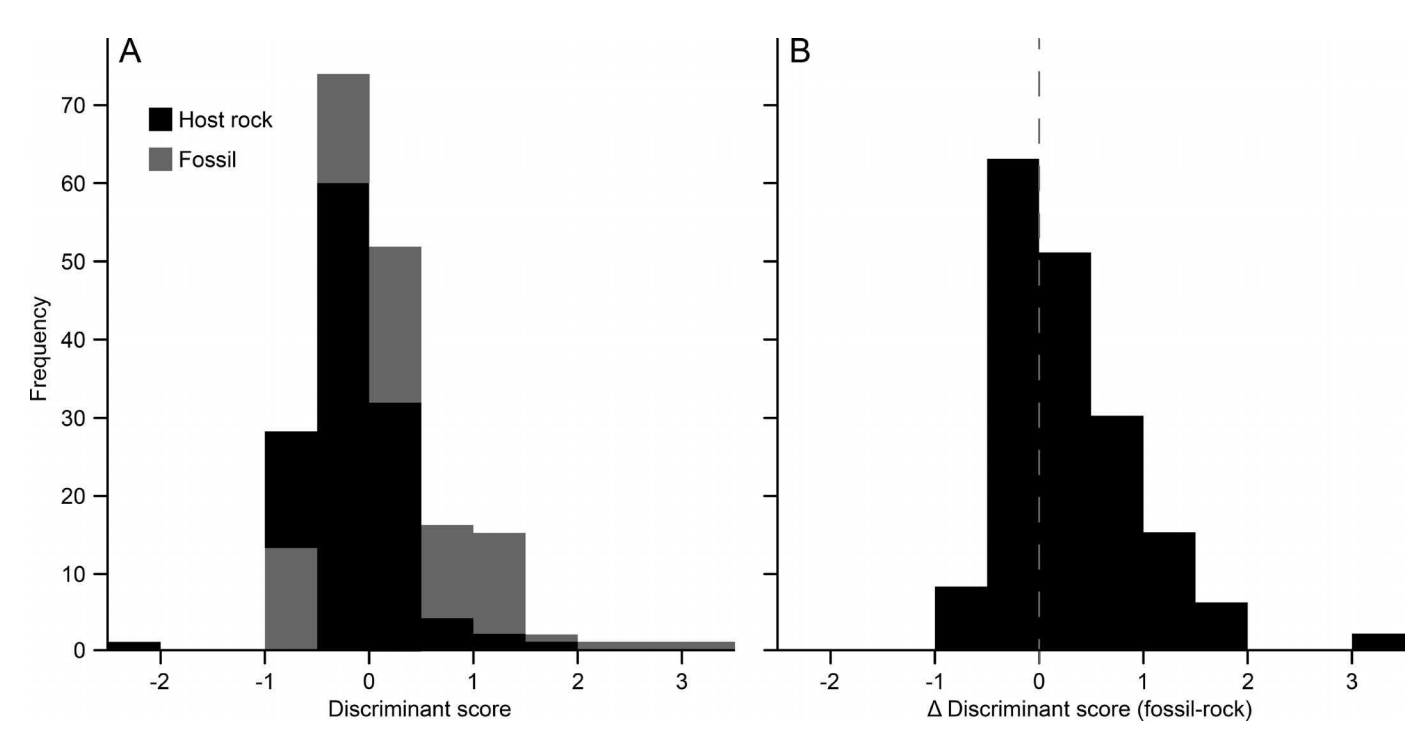


Fig. 7.—Discriminant analysis results. **A)** Discriminant scores of fossil (gray) and host rock (black); distributions are shown overlapping (not summed). **B)** Difference between each fossil discriminant score and the mean discriminant score of its host rock; vertical dashed line at 0 to aid viewing +/- Δ values and asymmetry of the distribution.

further beneath the surface of a specimen, resulting BSE images of thin film fossils likely contain signal from beneath (or within) the fossil film (e.g., Pang et al. 2013; Muscente and Xiao 2015b). This issue is exacerbated if the film is composed of low-density, low-atomic-numbercomprised materials like kerogen. Carbon has a very low backscatter coefficient (n; the proportion of beam electrons that are backscattered out of the specimen); as a fairly light element, carbon nuclei are not effective at changing the trajectory of a high-energy electron, which can result in electron transparency of thin carbonaceous materials at high accelerating voltages. Such a case is clearly observable here in KUMIP 314186-L, which contains framboidal pyrite entirely enveloped within its carbon film (Fig. 6E), yet still quite visible in BSE imaging. Monte Carlo simulations by Orr et al. (2002) suggest that carbon films even as small as 100 nm thick would be readily distinguishable from a silicate background based on its backscatter contrast at 5 keV. Even at 20 keV, the highest voltage used in this study, their simulations found there was still noticeable backscatter contrast at 500 nm thickness. Nonetheless, this is an important consideration for the specimens examined here.

612

Despite signal derived over a large interaction volume, EDS may be more effective than BSE imaging for detecting extremely thin carbon films. For instance, based on Monte Carlo simulations by Orr et al. (2009), a carbon film of only 200 Å thickness on a silicate substrate would be detectable in EDS at 5 keV. The study specimens, however, contain appreciable carbon in the host rock, and thus a greater thickness of carbon would be necessary to disentangle carbon-film signal from variations in the substrate. An example of this phenomenon can be observed in the EDS analyses of specimen KUMIP 204770-M at differing accelerating voltages (Table 2). On KUMIP 204770-M, a trend of decreasing carbon concentration with increasing accelerating voltage demonstrates that there is elevated carbon concentrations near the surface, but this is only clearly observed in areas with visible kerogen. Comparatively, other specimens, like KUMIP 314096-M, show somewhat elevated carbon concentrations in EDS analysis without visible kerogen. KUMIP 314096-M visually looks to be consistent with other kerogenized specimens (Fig. 1F); but upon BSE

inspection, only some annulations have visible kerogen, where others are broadly devoid of kerogen patches or other apparent carbon (Fig. 1G). Presumably, a carbon film, if present, may be too thin and electrontransparent for BSE imaging, but still provide optical contrast. While this may be a viable explanation, the carbon signal may alternatively be a result of elevated interstitial carbonaceous material in the fossil region as compared to the host rock. It is important to note that, with KUMIP 314096-M, the elevated carbon signal does not correspond to an elevated calcium signal, which could have instead indicated a fossil association with calcite (such as observed with KUMIP 314186-L, see Fig. 6F and later discussion). Such interstitial carbon, as hypothesized for KUMIP 314096-M, may be enough to alter the coloration of the host rock in the fossil region, giving the optical appearance of a continuous carbon film (Fig. 1F) but without SEM-visible carbonaceous remnants (Fig. 1G). This explanation may additionally apply to other fossils in this sample set as well, such as in the interannular spaces of KUMIP 204770-M.

Similarly, the electron beam interaction volume needs to be considered during EDS analysis of clay- and pyrite-associated examples. For instance, EDS analyses of clays in pyrite-bearing specimens often show higher average iron content in the clays of the fossil than those of the host rock, sometimes yielding iron content that is much higher than would be expected for a clay mineral. Yet, textural evidence does not show the presence of iron oxide minerals or pyrite. This could be the result of pyrite or other iron-bearing minerals buried underneath a thin layer of clay minerals. As mentioned above, in scanning electron microscopic analyses, beam electrons penetrate some depth into a specimen, which increases with increasing beam accelerating voltage, but only electrons that escape the specimen can be detected. As a result, the majority of the backscattered electron signal comes from relatively shallow parts of the specimen (although deeper than secondary electrons). However, the characteristic Xrays that are employed for EDS analysis escape the specimen from much deeper depths (and a greater three-dimensional volume) than BSEs or SEs, through the entirety of the beam interaction volume. Thus, EDS point analyses positioned in regions that do not appear to contain any pyrite based on backscattered electron imaging may still yield X-ray signal from veiled pyrite. We conducted Monte Carlo simulations using NIST DTSA-II to examine this possibility with an aluminosilicate mineral (Camontmorillonite). From our simulations, backscattered electrons may escape this material through $\sim 1~\mu m$ depth, but pyrite occurring as deep as $\sim 3~\mu m$ can impact the EDS elemental characterization. Thus, the iron signal common to many of the fossils analyzed here, and representing the largest positive elemental contributor to the discriminant analysis, may be in large part derived from iron minerals not immediately apparent on the surfaces of the fossils, but instead driven by buried pyrite and/or other iron-rich minerals within the upper few microns of the fossil material.

Preservation through Kerogenization

The fossils examined here that exhibit kerogenization as the primary mode of preservation are classified as representatives of the genus Ottoia (Fig. 1). There may be a taphonomic reason for this phenomenon. Ottoia and other priapulids have a recalcitrant chitinous cuticle (Schmidt-Rhaesa 2013), which may be histologically prone to detailed preservation via kerogenization. Annelid worms, for comparison, do not contain chitin in their cuticle (Richards 1978); while preserved through kerogenization, annelid fossils do not usually preserve cuticular details, though their chitinous chaetae are generally well-preserved (Wilson and Butterfield 2014). Consequently, some of the worm fossils with poor-fidelity kerogenization could be non-priapulids, which are poorly preserved due to histological-preservational biases. Alternately, because kerogenization exhibits higher biological fidelity compared, for instance, to pyritization, especially with regard to the preservation of taxonomically diagnostic surface features, the unidentifiable worms may also be Ottoia, but preserved through non-kerogenization pathways, thus limiting genus-level classification. More simply, in the studied specimens, kerogenization preserves greater anatomical detail than does pyritization. The unidentified vermiform fossils examined in this study are predominantly preserved via the latter, so the absence of taxonomically informative detail, and thus our ability for classification, could be a taphonomic artifact.

In KUMIP 298531-P, kerogen and framboidal pyrite closely correspond to original surficial features (Fig. 1D, 1E), such that the occurrence of kerogen patches and iron minerals are likely to have been driven by the surface geometry or histology of the deceased organism. Sulfate-reducing microbes convert organic carbon to bicarbonate ions, which eliminates the possibility of those carbon atoms becoming part of a carbonaceous compression. Thus, the presence of enhanced SRB-induced degradation in a certain part of the fossil would be expected to result in carbon being less abundant in that part of the fossil, and presumably with more pyriteassociation. However, the amount of kerogen in KUMIP 298531-P is not less in regions with localized pyrite-association than those without. This may be explained by taphonomic pathways occurring in different parts of the sediment column (Schiffbauer et al. 2014; Muscente et al. 2017), and the comparative recalcitrance of the tissues preserved via each pathway. SRBs readily and preferentially utilize the more labile organics of the decaying organism (Gabbott et al. 2004), but this may be decoupled from the degree of associated pyritization, which depends also on the availability of reduced iron. The more recalcitrant tissues that survive deeper within the sediment column, below the sulfate reduction zone, are preserved via kerogenization. Kerogenization exhibits patchiness in these fossils, where, between kerogen patches, there is very little carbon remaining such that the total quantity of carbon is miniscule compared to the amount originally in the worm. In these predominantly kerogenized fossils, pyrite is a minor constituent, and thus degradation by SRBs may not have been an important contributor to carbon loss (assuming that pyrite production was not otherwise limited, for instance, by a deficiency of reduced iron). The minor role of SRBs is further evidenced by the higher morphological fidelity of these kerogenized fossils as compared to those that are pyritized. With several different processes active during the taphonomic history of a given BST fossil, the drivers of carbon retention or loss and the production of pyrite (and other associated minerals) should be considered separately, though ultimately related to the chemistry of the burial microenvironment and rate of the fossil's progression through sedimentary microbial zones (Schiffbauer et al. 2014; Muscente et al. 2017).

The carbonaceous areas of these fossils, representing annulations and a gut tract, with high taphonomic fidelity of surface details suggest that microbial degradation of these tissues was minor. In priapulids, the annulations consist of circular bands of muscle with narrow gaps inbetween, and covered in integument (Schmidt-Rhaesa 2013). The transverse carbonaceous features of the fossils, specifically KUMIP 204770-M and 298531-P (Fig. 1A-1E) are very thin (50-100 μm), and may represent the spaces in-between annulations. The interannular spaces have considerably less muscular tissue, but considerably more integument, perhaps suggesting a higher, histologically driven potential for kerogenization of the integument. As observed in KUMIP 298531-P, these interpreted interannular spaces are also denoted by linear pyrite features, enveloped by a thin band of kerogen (Fig. 1E). Since the gut tract is comparably preserved, the wall of the gut may have similar properties. The surface of priapulid worm integument consists of an epidermis (high in lectin) above a layer of cuticle, which contains chitin, proteins, and polysaccharides (Schmidt-Rhaesa 2013). A similar tissue also coats the foregut, which can be introverted, but the midgut and foregut do not have a cuticular membrane (Schmidt-Rhaesa 2013). Because the surficial details of the fossil exist in patterns consistent with integument occurrence and structure (a relatively small fraction of the carbon of the total organism), the original histology of the integument is likely to have been more favorable for conversion to inert kerogen as compared to muscular tissues, and was sufficiently decay-resistant to retain fine detail until the onset of kerogenization. Chitin represents a convenient synthesis of these observations: it exists in the integument of priapulids (Schmidt-Rhaesa 2013), is resistant to microbial degradation (Sansom 2016), and becomes stable during diagenesis (Cody et al. 2011).

Two specimens, KUMIP 314111-L (Fig. 5C, 5D) and 314186-L (Fig. 6), exhibit a substantial, continuous carbon film. One unusual property of 314186-L is the cracks in the carbon film (Fig. 6B), which follow two orientations, irrespective of directional changes in the organism itself. This indicates that the fracture pattern is unrelated to the original anatomy of the organism, and originated instead after alteration of the carbon in the fossil.

Preservation through Pyritization

The fossils examined here that are preserved predominantly as pyriteassociated materials exhibit areas in which the concentration of pyrite framboids is elevated, commonly along the borders of the fossil (Fig. 2). This is possibly a product of geometric factors. Assuming a broadly cylindrical shape for a vermiform organism, with pyrite nucleating evenly across the surface of the organism while it still maintained some semblance of structural integrity early in the decay process, subsequent flattening would result in a concentration of pyrite along the borders of the compressed fossil and disseminated pyrite on the surface in-between. Annular features consisting of elevated concentrations of pyrite could be a result of pooled sulfides within interannular space (with more surface area in the entirety of a depression versus a flat surface) for pyrite nucleation. Pyritized annuli are most clearly observed in KUMIP 298531-P (Fig. 1E), but comparable features can also be observed in KUMIP specimens 377069-L (Fig. 2A-2C) and 314112-L (Fig. 4F). Both of these latter specimens, however, are catalogued as ichnofossils, and thus raise questions as to the biological nature of these pyritized annular features, which may instead be interpreted as backfill structures.

Some gut tracts also show elevated pyrite framboid concentrations around the borders of the gut, for instance KUMIP 377069-L (Fig. 2C) and

314159-L (Fig. 3A-3D), which may in effect be controlled by the same geometric factors as the localized pyritization along the body borders. Pyrite-association in the gut may be the inverse of pyrite-association on the dermis, where pyrite had encrusted the interior of a cylindrical cavity rather than the exterior of a cylindrical object. As such, the production of this style of gut tract preservation is presumably taphonomically early, likely requiring that the gut tract had not completely collapsed prior to the initiation of pyritization. Subsequent compression then produces a similar result to what is observed on the fossil body exteriors, with denser framboid distributions along the edges of the collapsed gut and disseminated on the compressed region between the edges. In specimens that have a pervasively and three-dimensionally pyritized gut tract, the gut must not have collapsed prior to initial pyrite formation. Further, much, if not most, of the pyrite formation occurred later in the diagenetic sequence, presumably from continued overgrowth of initial pyrite nucleation (Schiffbauer et al. 2014). In order for the three-dimensionality of the gut to be retained long enough for this to occur, the gut lining must have been stabilized by rapid, early pyritization, and a textural change should be observed to indicate continued mineral overgrowth later in the burial/ taphonomic sequence (Schiffbauer et al. 2014). Such a textural change is observed in KUMIP 314159-L, where botryoidal iron minerals overgrow euhedra (Fig. 3B). While this appears to be different than the textural change observed by Schiffbauer et al. (2014) in pyrite-infilled tubular fossils, it may nevertheless suggest two separate phases of pyrite mineralization, early onset and later overgrowth. The pyrite in the gut also encrusts large clay minerals (Fig. 3C, 3D) that are associated with much lower carbon content than those in the host rock. We consider it most likely that the clay minerals were within the gut prior to pyritization, likely via ingestion of sediment by an infaunal detritivore.

The origin of the extensively intergrowing euhedral pyrite texture found in KUMIP 293598-P (Fig. 2G) may be the result of pyrite recrystallization during diagenesis. The origin and identity of the small (240 nm) objects within the grains of pyrite framboids, such as in KUMIP 314202-L (Fig. 2E) remain unknown. In previous studies, such objects have been suggested to be bacteria (Rickard 2012). They are extremely small, even for bacteria, but might be small fragments of carbonaceous material. Alternatively, they may be small clay mineral particles, which would be consistent with pyrite appearing to overgrow clay booklets (e.g., Figs. 2G inset, 3C, 3D). Following the BST preservational model of Petrovich (2001), these small objects may represent biopolymers with adsorbed iron(II), in which case they may have served as nucleation sites for both iron(II)-rich clays and pyrite, and thus may play an integral role in fossil preservation via both pyrite-association (or more extensive pyritization) and aluminosilicification pathways.

KUMIP 314186-L (Fig. 6A) and 314111-L (Fig. 5C) both exhibit pyrite framboids trapped within carbon films (e.g., Fig. 6E), but no pyrite elsewhere in the specimens. It is possible that framboidal pyrite once existed elsewhere in this specimen, but was altered chemically and physically during weathering and/or diagenesis. Only the framboidal pyrite that remained within the possibly protective sheet of carbon survived. If this is the case, the alteration and removal of pyrite must have occurred after the alteration of the organic carbon to inert kerogen, otherwise these framboids would not have been protected.

The presence of pyrite-associated annular features in KUMIP 377069-L (Fig. 2A, 2B) and 314112-L (Fig. 4F), as well as pyritized medial features interpretable as gut tracts in KUMIP 377069-L (Fig. 2C) and 314202-L (Fig. 2D), may call into question the veracity of an ichnofossil assignment for these specimens, although our intent here is not to reclassify them. These and other expressed difficulties, however, highlight the complexity for resolving taxonomic (or even physiological) interpretations of relatively morphologically simple fossils. Further, these difficulties reinforce the need to resolve the possible histological-taphonomic interplay that permitted identification in the kerogenized priapulid specimens.

Preservation through Aluminosilicification

The clay compositions of specimens KUMIP 293611-P (Fig. 4A), 314215-L (Fig. 3E), and 314186-L (Fig. 6) strongly differ between the fossil and host-rock matrix. In the case of KUMIP 293611-P, the texture of the fossil clays is very fine and randomly oriented, which could represent a primary association. In other examples, such as one of the Ottoia specimens KUMIP 204770-M, while clay compositions between the host rock and fossil may be comparable, the clay texture differs (Fig. 1C). The contrast between the rough, randomly oriented clays of the host rock and the smooth, preferentially oriented clays on the fossil surface may indicate authigenic clay mineral growth or detrital deposition followed by compaction on the smooth fossil surface—in either case, representing an early, possibly taphonomically constructive association of these clays. In KUMIP 314186-L, the clays consist of needles oriented perpendicular to a carbon film (Fig. 6G), and thus could be an example of a void-filling ironrich clay growing on the carbon film. Its textural properties, however, are unique within the material sampled in this study; the same processes may not be responsible for the clays elsewhere in either this specimen or others.

The analyzed material contains fossils with very diverse host rock compositions and diverse preservational styles, which makes it difficult to identify overall trends. While it is tempting to look at the taphonomic variation by locality, the differences in host rock compositions between individual specimens, even at the same locality, may be greater than the differences between fossil and host rock in individual specimens, which can conceal much of the taphonomic signal. The discriminant analysis elucidated significant differences in composition between fossils and their respective host rocks. This is particularly remarkable because the fossils are preserved as thin films on bedding surfaces and the compositional data is collected from a volume of material that extends beyond the fossil and into the rock. Indeed, volumetrically, the majority of the data is acquired from the underlying rock. While there is a significant difference between the central tendencies of fossil and rock composition, the fact that compositional signal is assessed from (nearly) the whole of the interaction volume yields considerable overlap in their dispersion. This large variation undoubtedly contributes to the seemingly low percentage of correct a posteriori reclassification (58.42%) based upon the discriminant function. However, it should be noted that a 58.42% correct reclassification rate from 303 observations (177 reclassified correctly) is significantly higher than what one would expect from simply having a 50% probability of correctly choosing between two groups (Binomial test p = 0.0039). The discriminant analysis showed that all but one of the fossils (with KUMIP 314111-L the exception) showed higher discriminant scores than the host rock (Fig. 7, Table 3). With iron having a strong positive influence, the elevated concentration of pyrite could be responsible for higher discriminant scores at least in some specimens, but fossils devoid of any visible pyrite still show higher discriminant scores. As such, there must be another underlying reason for the consistency of composition across these specimens, such as taphonomic clay association (Orr et al. 1998) or iron oxide infiltration (Gaines 2014).

Calcium Associations and Phosphatization

Calcium can occur in clay minerals, such as smectites like montmorillonite, which may be a viable explanation for the calcium associations in at least some of the analyzed specimens. Others, however, appear to be associated with small amounts of calcium carbonate. One specimen, KUMIP 314186-L, contains a surficial calcium carbonate crust on part of the fossil (Fig. 6F). This crust may be weathering-related, considering the proximity of overlying calcium carbonate silts. However, while the visible calcite in KUMIP 314186-L appears to be later, there is also elevated calcium in points along the gut that are not near visible calcite. Another specimen, KUMIP 314107-L, shows extensive phosphatization (Fig. 5A,

5B). Phosphatization in BST fossils is well described, but typically in reference to preservation of gut tracts or midgut glands (Butterfield 2002; Lerosey-Aubril et al. 2012). If this specimen is a phosphatized gut tract, it shows no trace of the body of the organism, either optically or using microanalytical techniques. A possible, and perhaps likely alternative interpretation is that it instead represents a phosphatized coprolite. Although reports of Cambrian coprolites are not extensive (Vannier and Chen 2005; Eriksson and Terfelt 2007; Kimmig and Strotz, 2017), some are phosphatized, albeit much smaller fecal materials (Shen et al. 2014).

In addition to the above mechanisms for calcium associations, calcium carbonate precipitation may be facilitated by sulfate-reducing microbes. The metabolism of SRBs converts organic carbon to free bicarbonate (HCO₃⁻) ions. Depending on what organic compounds are being metabolized and how completely they are metabolized, pH may rise or fall. In circumstances where hydrogen sulfide can escape from the system, pH will rise. The increase in alkalinity from the introduction of bicarbonate and the increase of pH would make precipitation of calcium carbonate more favorable (Gallagher et al. 2012). In microbial mats where over half of the organic carbon produced by autotrophs becomes metabolized by sulfate-reducing bacteria, authigenic calcium carbonate is commonly precipitated (Gallagher et al. 2012). As sulfate reduction has clearly played a role in the degradation of many of these worms, the calcium anomalies may be a result of small amounts of precipitated calcium carbonate from the activity of SRBs. Aside from KUMIP 314107-L (the fully phosphatized specimen) and KUMIP 314186-L (with the calcite crust), all of the specimens that show elevated calcium concentrations also show pyrite association, which may intimate the role of bacterial sulfate reduction in calcium carbonate association.

Monazite Associations

Other than for one occurrence in the Pioche Shale (Moore and Lieberman 2009), monazite has not been reported previously in association with BST fossils. Monazite is a light rare-earth-element-(LREE)-bearing phosphate abundant in cerium, lanthanum, and neodymium as well as other elements, such as thorium, in low abundance (Spear and Pyle 2002). Monazite often occurs in association with apatite, forming during metasomatic dissolution of LREE-bearing apatite. This reaction has been observed in the laboratory at simulated greenschist-grade conditions, but has occurred in nature at temperatures as low as 100°C (Harlov and Förster 2003). Apatite is therefore a plausible precursor for the monazites in specimens KUMIP 314114-L (Fig. 5E–G) and 314186-L (Fig. 6B–D), given that phosphatic preservation of gut tracts is somewhat commonplace.

Barite Associations

Several specimens show barite within the fossil material. KUMIP 314111-L (Fig. 5C) exhibits abundant, bladed barite around the exterior of the fossil (Fig. 5D). KUMIP 314191-L (an unknown animal; Fig. 5I) contains barite as needle-shaped crystals (Fig. 5J) as well as a relatively high titanium content (10.1 at. %). As previously mentioned, KUMIP 314215-L shows barite encrusting a portion of the fossil's gut tract (Fig. 3E, 3F). Like iron, barium is a redox-sensitive metal that is mobile in anoxic waters. In environments where SRBs have converted the majority of sulfates to sulfides, barium becomes mobile, but will not precipitate as barite until sulfate-rich conditions return (Paytan et al. 2004). Fossils containing barite have been observed previously (Nuelle and Shelton 1986; Wilby et al. 1996; Muscente and Xiao 2015a), but no mechanism for the primary association of barite with soft-tissues has been suggested. In this case, barite could be an altered form of another taphonomic mineral, such as pyrite. Oxidation of the associated pyrite produces dissolved sulfate ions that could prompt local, later, diagenetic precipitation of barite (Hanor 2000). One other specimen, KUMIP 314096-M (Fig. 1F), contains large patches of bladed barite encrusting the surface of the fossil (Fig. 1H). These features do not seem to have any spatial pattern relative to fossil morphology, and thus are likely not related to early diagenetic, preservationally active fossil association.

Iron and Manganese Oxide Banding

KUMIP 293611-P exhibits a unique pattern of alternating iron and manganese oxides near one end of the fossil (Fig. 4D, 4E). Any primary taphonomic processes that could produce such a pattern are unknown. We propose that the formation of this Fe-Mn feature roughly coincided with the oxidation of pyrite, which may have resulted in iron mobilization and precipitation as an oxide. Manganese is another redox-sensitive transition metal, with similar properties to iron (Nealson 1997), so the formation of this feature may have been controlled by minor fluctuations in Eh-pH conditions during oxidative weathering.

SYNTHESIS AND REVIEW

Despite the remarkable variety of taphonomic styles in the vermiform fossils of the Great Basin, including individual specimens showing diverse mineralization patterns, all can be broadly reconciled in a single model (Fig. 8).

The fossil material of this study is likely to have been rapidly buried shortly following, or concomitant with, death of the organism. Some of the specimens show evidence of burial by distal turbidites, as evidenced by graded bedding (e.g., Fig. 6F). It is possible that others were not buried in turbidites, but, instead, were already beneath the sediment surface at the time of death, given that an infaunal life mode is common among worms. In such cases, rapid sedimentation would have cut off oxygen supply to these burrowers, smothered them and simultaneously begun the taphonomic process.

Sulfate-reducing microbes, both in the gut and in the sediment, were important decomposers of these organisms. The resulting bisulfide, with porewater reduced iron, formed the precursors to pyrite in framboidal and euhedral crystal habits at nucleation sites—possibly at loci where iron(II) had adsorbed onto decaying organics (Petrovich 2001). Certain geometric factors influence the location of pyrite precipitation, including annulations (e.g., Figs. 1E, 2B) and digestive tracts (e.g., Fig. 2C), which serve to concentrate sulfide ions. Organisms whose life mode involved ingesting sediment may have the digestively altered sediment particles within their guts surrounded by iron minerals (Fig. 3C, 3D). Pending appropriate conditions, potentially influenced by porosity, the products of sulfatereducing microbe metabolisms may favor precipitation of small amounts of calcium carbonate in the interstitial spaces near the remains (Gallagher et al. 2012). This would serve to reduce the porosity of the sediment (e.g., Gaines et al. 2012), which would further limit the diffusion of oxidative ions like sulfate that microbes require for their metabolism, and ensure that some carbon is retained for later kerogenization after further burial. Lipids and chitin would remain relatively intact (Briggs et al. 2000), owing to the difficulty of metabolizing such biopolymers (especially without an electron acceptor as effective as oxygen). The presence of chitin in priapulid worms may have inhibited degradation of fine morphological detail from microbial decay. If pH in the gut becomes low, then some dissolved calcium and phosphate may precipitate in the form of apatite within the gut tract, nucleating on microbes or tissues (Wilby and Briggs 1997). When available sulfate is exhausted, methanogenic organisms may continue to degrade the organism, but would still experience difficulty breaking down lipids and chitin. If anoxic conditions are disrupted, some pyrite particles may partially dissolve, enriching the surrounding clays in iron (Gaudin et al. 2005). Initial pyritization may have been limited in scope, especially in restricted environments like gut tracts. Some pyrite overgrowth (Fig. 3B,

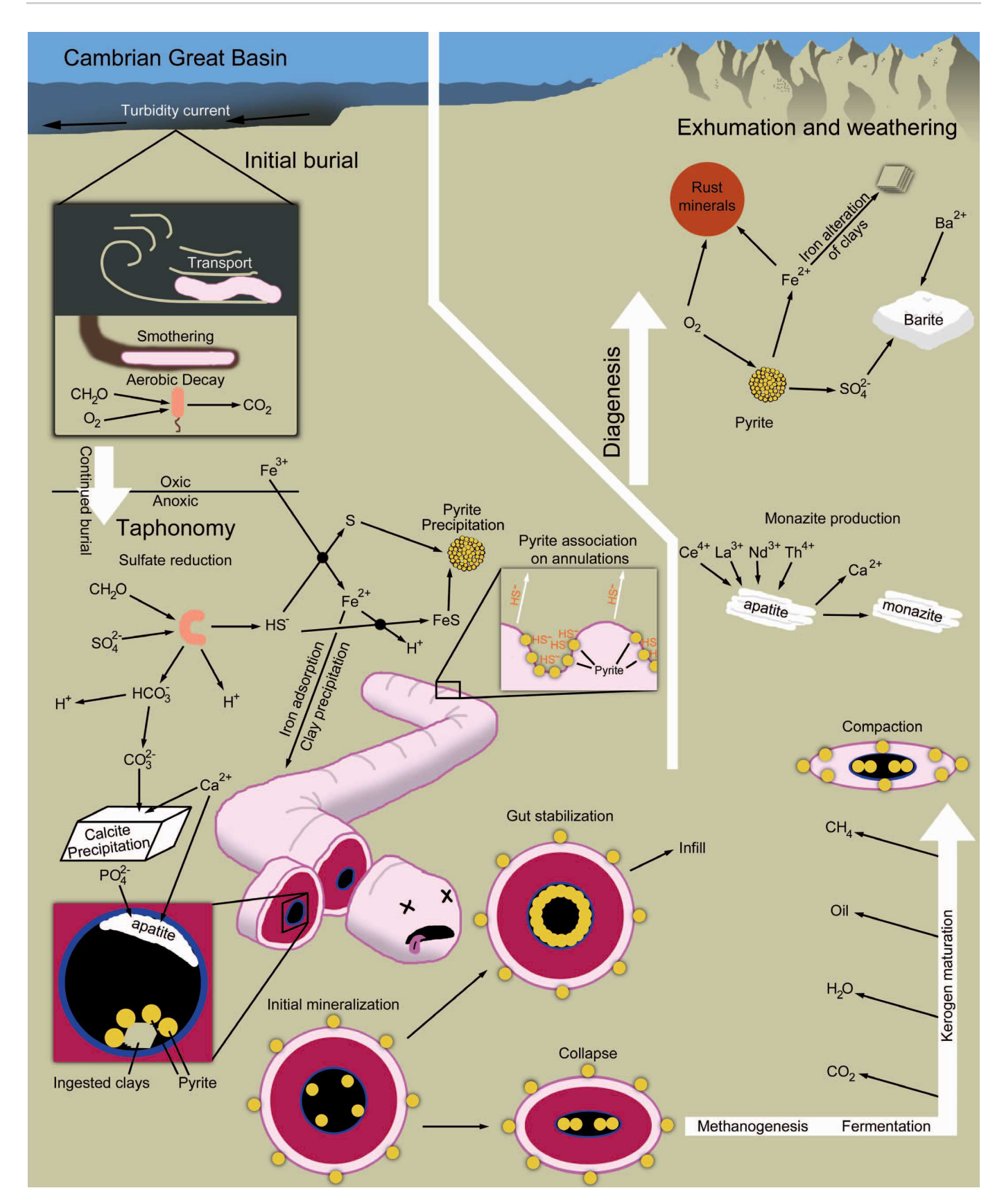


Fig. 8.—Generalized model of taphonomic and later diagenetic processes (burial, taphonomic mineralization, collapse and compaction, diagenesis, and exhumation and weathering) that cumulatively affected fossil preservation of Great Basin vermiform fossils.

3D) very likely continued after decay of the organism had ceased (Schiffbauer et al. 2014).

Eventually, decay-induced loss of tissue structural integrity would lead to collapse, and compaction of the host sediments would cause further compression. Where the shape of an organism had been stabilized by minerals, it may retain its shape long enough for later mineralization to fill the void spaces—comparable to pervasive, three-dimensional pyritization of some interpreted gut tracts here. If enough carbon remains enveloping gut-tract minerals, it may serve to protect those minerals from later alteration (Fig. 6E). Pending thermal maturation, which deposits in the Great Basin are known to have undergone (Bernard and Horsfield 2014), any remaining solid organic carbon can be converted to lower-oxygen and lower-hydrogen forms of inert kerogen (Muscio and Horsfield 1996; Schopf et al. 2005; Schiffbauer et al. 2012). All of these processes produce a reduction in volume. In the chitin-bearing priapulid fossils, the chitin eventually becomes inert kerogen, sometimes exhibiting a cracked texture (Fig. 1C), an expected product of volumetric reduction. In other fossils, some void space may have been produced via this process, which could be filled by other minerals later in the diagenetic sequence. Priapulids may have exhibited preferential preservation of fine morphological structures in inert kerogen (Fig. 1A-1E), due to their cuticular chitin. The taxonomy of the majority of fossils in this study is unresolved with only the unequivocal priapulids having fine morphological detail preserved via kerogenization.

Eventually, the processes of diagenesis and weathering impacted the composition of the clays of the host rock, and converted pyrite to iron oxides. Barium-rich fluids may alter pyrite to barite (e.g., Figs. 3F, 5D), and LREE-rich fluids may alter apatite to monazite (e.g., Fig. 5G). Void spaces could be filled by late diagenetic iron oxides (e.g., Fig. 4D, 4E), calcium carbonate, barite (Fig. 1H), or clay minerals (Fig. 6G). Certain mineral grains may escape alteration, provided that they are isolated from fluids. This is evident especially in the clays of the gut of KUMIP 314159-L (Fig. 3C, 3D) and the pyrite within the carbon of KUMIP 314186-L (Fig. 6E).

As signified in the discriminant analysis, specimens in this study exhibit evidence of differential clay composition between the fossil and host rock. Of these, KUMIP 293611-P is the most significant, exhibiting high ironrich clay compositions (Fig. 4A, 4B). It is unclear whether these clays originated as authigenic clays, diagenetically altered detrital clays, or void-filling late-stage clays, although broad similarities in fossil-clay and host rock compositions may support a detrital origin. Nonetheless, the vermiform fossils examined from the Great Basin do not exhibit contrasts in clay mineral composition between fossil and matrix as strongly as other, previously examined BST fossils (e.g., Orr et al. 1998). Life mode (deposit feeding versus other) and/or histological biochemistry may play significant roles in the mode of clay mineral associations, if taphonomically constructive (aiding in preservation).

CONCLUSIONS

Although preservation of the fossils shown here can be broadly defined as Burgess Shale-type, there are many variations on this general taphonomic theme. Many of these fossils were extracted from the same formation and same locality, presumably with cursorily similar postmortem conditions from burial and decay to diagenesis. Indeed, even fossils from different localities and formations examined here were interred in similar sedimentary settings in the same basin at around the same time, thus likely experiencing the same general "distal" paleoenvironmental conditions (sensu Cai et al. 2012). While cognizant of the fact that microenvironmental or bed-by-bed conditions may change over time, we can generalize a consistent suite of processes to explain the preservation of each of these worms. Pyritization begins concurrently with decay by sulfur-reducing bacteria and, in initial stages, represents a small quantity of pyrite, which can effectively stabilize the void space from compaction and allow for later pyrite overgrowth. Calcite and apatite can precipitate as other by-products

of decay. Kerogenization, as observed in previous studies (e.g., Gabbott et al. 2004) preserves only the most decay-resistant tissues, in this case cuticular chitin. Late-stage alteration chemically changes minerals precipitated during initial taphonomic stages. While this alteration obscures the possible original role of some taphonomically constructive minerals, the changes can largely be geochemically explained. Variations between specimens can be explained as the manifestations of minor variations in microenvironmental conditions during burial, decay, diagenesis, and oxidation, all of which exist under a common framework of BST processes. Other localities of Burgess Shale-type preservation may exhibit overall differences in the taphonomic and diagenetic path, but we suggest that these differences will likely be consistent with the mechanisms discussed in this study.

ACKNOWLEDGMENTS

The authors would like to acknowledge the laboratory assistance of E.M. Schneider; the University of Missouri Electron Microscopy Core facility; and J.W. Huntley and K.L. Shelton for discussion. We thank the Kansas Biodiversity Institute, Ú.C. Farrell, M.M. Casey, J. Kimmig, and B.S. Lieberman for collections assistance, as well as M. Laflamme and two anonymous reviewers, who greatly improved the quality of this report. JDS acknowledges the Donors of the American Chemical Society Petroleum Research Fund (PRF# 53833-DNI8) and the NSF Faculty Early Career Development Program (CAREER Award# 1652351) for support of this research.

SUPPLEMENTAL MATERIAL

Data are available from the PALAIOS Data Archive: http://www.sepm.org/pages.aspx?pageid=332.

REFERENCES

Anderson, E.P., Schiffbauer, J.D., and Xiao, S., 2011, Taphonomic study of organic-walled microfossils confirms the importance of clay minerals and pyrite in Burgess Shale-type preservation: Geology, v. 39, p. 643–646.

Bernard, S. and Horsfield, B., 2014, Thermal maturation of gas shale systems: Annual Review of Earth and Planetary Sciences, v. 42, p. 635–651.

Berner, R.A., 1984, Sedimentary pyrite formation: an update: Geochimica et Cosmochimica Acta, v. 48, p. 605–615.

Brett, C.E., Allison, P.A., DeSantis, M.K., Liddell, W.D., and Kramer, A., 2009, Sequence stratigraphy, cyclic facies, and lagerstätten in the middle Cambrian Wheeler and Marjum Formations, Great Basin, Utah: Palaeogeography, Palaeoclimatology, Palaeoecology, v. 277, p. 9–33.

BRIGGS, D.E.G., EVERSHED, R.P., AND LOCKHEART, M.J., 2000, The biomolecular paleontology of continental fossils: Paleobiology, v. 26, p. 169–193.

BRIGGS, D.E.G., LIEBERMAN, B.S., HENDRICKS, J.R., HALGEDAHL, S.L., AND JARRARD, R.D., 2008, Middle Cambrian arthropods from Utah: Journal of Paleontology, v. 82, p. 238– 254, doi: 10.1666/06-086.1.

BRIGGS, D.E.G. AND MOUNT, J.D., 1982, The occurrence of the giant arthropod Anomalocaris in the lower Cambrian of southern California, and the overall distribution of the genus: Journal of Paleontology, v. 56, p. 1112–1118.

BRIGGS, D.E.G. AND NEDIN, C., 1997, The taphonomy and affinities of the problematic fossil Myoscolex from the lower Cambrian Emu Bay shale of south Australia: Journal of Paleontology, v. 71, p. 22–32.

BRIGGS, D.E.G., RAISWELL, R., BOTTRELL, S.H., HATFIELD, D., AND BARTELS, C., 1996, Controls on the pyritization of exceptionally preserved fossils: an analysis of the Lower Devonian Hunsrueck Slate of Germany: American Journal of Science, v. 296, p. 633– 662

BUTTERFIELD, N.J., 1995, Secular distribution of Burgess Shale-type preservation: Lethaia, v. 28, p. 1–13.

BUTTERFIELD, N.J., 2002, Leanchoilia guts and the interpretation of three-dimensional structures in Burgess Shale-type fossils: Paleobiology, v. 28, p. 155–171, doi: 10.1666/00 94-8373(2002)028<0155:lgatio>2.0.co;2.

BUTTERFIELD, N.J., 2003, Exceptional fossil preservation and the Cambrian explosion: Integrative and Comparative Biology, v. 43, p. 166–177, doi: 10.1093/icb/43.1.166.

CAI, Y., SCHIFFBAUER, J.D., HUA, H., AND XIAO, S., 2012, Preservational modes in the Ediacaran Gaojiashan Lagerstätte: pyritization, aluminosilicification, and carbonaceous compression: Palaeogeography, Palaeoclimatology, Palaeoecology, v. 326–328, p. 109– 117.

- Canfield, D.E. and Raiswell, R., 1991, Pyrite formation and fossil preservation, *in P.A.* Allison and D.E.G. Briggs (eds.), Taphonomy; Releasing the Data Locked in the fossil Record: Plenum Press, New York, NY, p. 337–387.
- Cody, G.D., Gupta, N.S., Briggs, D.E., Kilcoyne, A., Summons, R.E., Kenig, F., Plotnick, R.E., and Scott, A.C., 2011, Molecular signature of chitin-protein complex in Paleozoic arthropods: Geology, v. 39, p. 255–258.
- Conway Morris, S. and Robison, R.A., 1986, Middle Cambrian priapulids and other soft-bodied fossils from Utah and Spain: The University of Kansas Paleontological Contributions, v. 117, p. 1–22.
- Conway Morris, S. and Robison, R.A., 1988, More soft-bodied animals and algae from the middle Cambrian of Utah and British Columbia: The University of Kansas Paleontological Contributions, v. 122, p. 23–84.
- Donald, R. and Southam, G., 1999, Low temperature anaerobic bacterial diagenesis of ferrous monosulfide to pyrite: Geochimica et Cosmochimica Acta, v. 63, p. 2019–2023.
- ELRICK, M. AND SNIDER, A.C., 2002, Deep-water stratigraphic cyclicity and carbonate mud mound development in the middle Cambrian Marjum Formation, House Range, Utah, USA: Sedimentology, v. 49, p. 1021–1047.
- Eriksson, M.E. and Terfelt, F., 2007, Anomalous facies and ancient faeces in the latest middle Cambrian of Sweden: Lethaia, v. 40, p. 69–84.
- FARRELL, Ú.C., 2014, Pyritization of soft-tissues in the fossil record: an overview: Paleontological Society Papers, v. 20, p. 35–57.
- Forchielli, A., Steiner, M., Hu, S.X., and Keupp, H., 2012, Taphonomy of Cambrian (Stage 3/4) sponges from Yunnan (South China): Bulletin of Geosciences, p. 133–142, doi: 10.3140/bull.geosci.1225.
- FORCHIELLI, A., STEINER, M., KASBOHM, J., Hu, S., AND KEUPP, H., 2014, Taphonomic traits of clay-hosted early Cambrian Burgess Shale-type fossil Lagerstätten in South China: Palaeogeography, Palaeoclimatology, Palaeoecology, v. 398, p. 59–85, doi: 10.1016/j. palaeo.2013.08.001.
- Gabbott, S.E., Hou, X.G., Norry, M.J., and Siveter, D.J., 2004, Preservation of early Cambrian animals of the Chengjiang biota: Geology, v. 32, p. 901–904.
- Gaines, R.R., 2014, Burgess Shale-type preservation and its distribution in space and time: Paleontological Society Papers, v. 20, p. 123–146.
- GAINES, R.R., BRIGGS, D.E.G., AND YUANLONG, Z., 2008, Cambrian Burgess Shale–type deposits share a common mode of fossilization: Geology, v. 36, p. 755–758.
- GAINES, R.R. AND DROSER, M.L., 2010, The paleoredox setting of Burgess Shale-type deposits: Palaeogeography Palaeoclimatology Palaeoecology, v. 297, p. 649–661, doi: 10.1016/j.palaeo.2010.09.014.
- GAINES, R.R., HAMMARLUND, E.U., HOU, X., QI, C., GABBOTT, S.E., ZHAO, Y., PENG, J., AND CANFIELD, D.E., 2012, Mechanism for Burgess Shale-type preservation: Proceedings of the National Academy of Sciences, v. 109, p. 5180–5184.
- GALLAGHER, K.L., KADING, T.J., BRAISSANT, O., DUPRAZ, C., AND VISSCHER, P.T., 2012, Inside the alkalinity engine: the role of electron donors in the organomineralization potential of sulfate-reducing bacteria: Geobiology, v. 10, p. 518–530.
- GARSON, D.E., GAINES, R.R., DROSER, M.L., LIDDELL, W.D., AND SAPPENFIELD, A., 2012, Dynamic palaeoredox and exceptional preservation in the Cambrian Spence Shale of Utah: Lethaia, v. 45, p. 164–177, doi: 10.1111/j.1502-3931.2011.00266.x.
- GAUDIN, A., BUATIER, M.D., BEAUFORT, D., PETIT, S., GRAUBY, O., AND DECARREAU, A., 2005, Characterization and origin of Fe3+-montmorillonite in deep-water calcareous sediments (Pacific Ocean, Costa Rica margin): Clays and Clay Minerals, v. 53, p. 452-465.
- GOLDSTEIN, J.I., NEWBURY, D.E., JOY, D.C., LYMAN, C.E., ECHLIN, P., LIFSHIN, E., SAWYER, L., AND MICHAEL, J.R., 2003, Scanning Electron Microscopy and X-Ray Microanalysis (3rd edition): Springer, New York, 689 p.
- GUPTA, N.S., MICHELS, R., BRIGGS, D.E., EVERSHED, R.P., AND PANCOST, R.D., 2006, The organic preservation of fossil arthropods: an experimental study: Proceedings of the Royal Society of London B: Biological Sciences, v. 273, p. 2777–2783.
- Hammer, Ø., Harper, D.A.T., and Ryan, P.D., 2001, PAST. Paleontological Statistics Software Package for Education and Data Analysis: Palaeontologia Electronica, v. 4. http://palaeo-electronica.org/2001_1/past/issue1_01.htm
- HANOR, J.S., 2000, Barite-celestine geochemistry and environments of formation: Reviews in Mineralogy and Geochemistry, v. 40, p. 193–275.
- HARLOV, D.E. AND FÖRSTER, H.-J., 2003, Fluid-induced nucleation of (Y+ REE)-phosphate minerals within apatite: nature and experiment, Part II, fluorapatite: American Mineralogist, v. 88, p. 1209–1229.
- HUNGER, S. AND BENNING, L.G., 2007, Greigite: a true intermediate on the polysulfide pathway to pyrite: Geochemical transactions, v. 8, p. 1.
- KIMMIG, J. AND STROTZ, L.C., 2017, Coprolites in mid-Cambrian (Series 2-3) Burgess Shaletype deposits of Nevada and Utah and their ecological implications: Bulletin of Geosciences, v. 92, p. 297–309.
- KLOSS, T.J., DORNBOS, S.Q., CHEN, J.-Y., McHENRY, L.J., AND MARENCO, P.J., 2015, Highresolution geochemical evidence for oxic bottom waters in three Cambrian Burgess Shale-type deposits: Palaeogeography, Palaeoclimatology, Palaeoecology, v. 440, p. 90– 95
- KONHAUSER, K.O., 1998, Diversity of bacterial iron mineralization: Earth-Science Reviews, v. 43, p. 91–121.
- Lerosey-Aubril, R., Hegna, T.A., Kier, C., Bonino, E., Habersetzer, J., and Carre, M., 2012, Controls on gut phosphatisation: the trilobites from the Weeks Formation Lagerstatte (Cambrian; Utah): PLoS ONE, v. 7, p. e32934, doi: 10.1371/journal. pone.0032934.

- LIEBERMAN, B.S., 2003, A new soft-bodied fauna: the Pioche Formation of Nevada: Journal of Paleontology, v. 77, p. 674–690.
- LIN, J.-P. AND BRIGGS, D.E.G., 2010, Burgess Shale-type preservation: a comparison of Naraoiids (Arthropoda) from three Cambrian localities: PALAIOS, v. 25, p. 463–467.
- McMahon, S., Anderson, R.P., Saupe, E.E., and Briggs, D.E.G., 2016, Experimental evidence that clay inhibits bacterial decomposers: Implications for preservation of organic fossils: Geology, v. 44, p. 867–870, doi: 10.1130/g38454.1.
- MOORE, R.A. AND LIEBERMAN, B.S., 2009, Preservation of early and middle Cambrian soft-bodied arthropods from the Pioche Shale, Nevada, USA: Palaeogeography, Palaeoclimatology, Palaeoecology, v. 277, p. 57–62.
- MUSCENTE, A.D., HAWKINS, A.D., AND XIAO, S., 2015, Fossil preservation through phosphatization and silicification in the Ediacaran Doushantuo Formation (South China): a comparative synthesis: Palaeogeography, Palaeoclimatology, Palaeoecology, v. 434, p. 46–62.
- Muscente, A.D., Schiffbauer, J.D., Broce, J., Laflamme, M., O'Donnell, K., Boag, T.H., Meyer, M., Hawkins, A.D., Huntley, J.W., McNamara, M., MacKenzie, L.A., Stanley Jr., G.D., Hinman, N.W., Hoffman, M.H., and Xiao, S., 2017, Exceptionally preserved fossil assemblages through geologic time and space: Gondwana Research, v. 48, p. 164–188.
- Muscente, A.D. and Xiao, S., 2015a, New occurrences of *Sphenothallus* in the lower Cambrian of South China: Implications for its affinities and taphonomic demineralization of shelly fossils: Palaeogeography, Palaeoclimatology, Palaeoecology, v. 437, p. 141–146, doi: 10.1016/j.palaeo.2015.07.041.
- Muscente, A.D. and Xiao, S., 2015b, Resolving three-dimensional and subsurficial features of carbonaceous compressions and shelly fossils using backscattered electron scanning electron microscopy (BSE-SEM): PALAIOS, v. 30, p. 462–481.
- MUSCIO, G.P. AND HORSFIELD, B., 1996, Neoformation of inert carbon during the natural maturation of a marine source rock: Bakken Shale, Williston Basin: Energy and Fuels, v. 10, p. 10–18.
- NEALSON, K.H., 1997, Sediment bacteria: who's there, what are they doing, and what's new?: Annual Review of Earth and Planetary Sciences, v. 25, p. 403–434.
- NUELLE, L.M. AND SHELTON, K.L., 1986, Geologic and geochemical evidence of possible bedded barite deposits in Devonian rocks of the Valley and Ridge Province, Appalachian Mountains: Economic Geology, v. 81, p. 1408–1430.
- ORR, P.J., BRIGGS, D.E.G., AND KEARNS, S.L., 1998, Cambrian Burgess Shale animals replicated in clay minerals: Science, v. 281, p. 1173–1175, doi: 10.1126/science.281.53 80.1173.
- ORR, P.J. AND KEARNS, S.L., 2011, X-ray microanalysis of Burgess Shale and similarly preserved fossils, *in* M. Laflamme, J.D. Schiffbauer, and S.Q. Dornbos (eds.), Quantifying the Evolution of Early Life: Numerical Approaches to the Evaluation of Fossils and Ancient Ecosystems: Springer, Netherlands, p. 271–300.
- ORR, P.J., KEARNS, S.L., AND BRIGGS, D.E.G., 2002, Backscattered electron imaging of fossils exceptionally preserved as organic compressions: PALAIOS, v. 17, p. 110–117.
- ORR, P.J., KEARNS, S.L., AND BRIGGS, D.E.G., 2009, Elemental mapping of exceptionally preserved 'carbonaceous compression' fossils: Palaeogeography, Palaeoclimatology, Palaeoecology, v. 277, p. 1–8.
- PAGE, A., GABBOTT, S.E., WILBY, P.R., AND ZALASIEWICZ, J.A., 2008, Ubiquitous Burgess Shale–style "clay templates" in low-grade metamorphic mudrocks: Geology, v. 36, p. 855–858, doi: 10.1130/g24991a.1.
- PALMER, A., 1998, Terminal early Cambrian extinction of the Olenellina: documentation from the Pioche Formation, Nevada: Journal of Paleontology, v. 72, p. 650–672.
- Pang, K., Tang, Q., Schiffbauer, J.D., Yao, J., Yuan, X., Wan, B., Chen, L., Ou, Z., and Xiao, S., 2013, The nature and origin of nucleus-like intracellular inclusions in Paleoproterozoic eukaryote microfossils: Geobiology, v. 11, p. 499–510.
- PAYTAN, A., MARTINEZ-RUIZ, F., EAGLE, M., IVY, A., AND WANKEL, S., 2004, Using sulfur isotopes to elucidate the origin of barite associated with high organic matter accumulation events in marine sediments: Geological Society of America Special Papers, v. 379, p. 151–160.
- Petrovich, R., 2001, Mechanisms of fossilization of the soft-bodied and lightly armored faunas of the Burgess Shale and of some other classical localities: American Journal of Science, v. 301, p. 683–726.
- POWELL, W., 2003, Greenschist-facies metamorphism of the Burgess Shale and its implications for models of fossil formation and preservation: Canadian Journal of Earth Sciences, v. 40, p. 13–25, doi: 10.1139/e02-103.
- RAFF, E.C., SCHOLLAERT, K.L., NELSON, D.E., DONOGHUE, P.C.J., THOMAS, C.-W., TURNER, F.R., STEIN, B.D., DONG, X.-P., BENGTSON, S., HULDTGREN, T., STAMPANONI, M., CHONGYU, Y., AND RAFF, R.A., 2008, Embryo fossilization is a biological process mediated by microbial biofilms: Proceedings of the National Academy of Sciences USA, v. 105, p. 19360–19365.
- RAFF, R.A. AND RAFF, E.C., 2014, The role of biology in the fossilization of embryos and other soft bodied organisms: microbial biofilms and Lagerstätten: Paleontological Society Papers, v. 20, p. 83–100.
- REES, M., 1986, A fault-controlled trough through a carbonate platform: The middle Cambrian House Range embayment: Geological Society of America Bulletin, v. 97, p. 1054–1069.
- $R_{ICHARDS},\,K.,\,1978,\,Epidermis\,\,and\,\,cuticle:\,Physiology\,\,of\,\,annelids,\,v.\,\,33,\,p.\,\,61.$
- RICKARD, D., 2012, Sulfidic sediments and sedimentary rocks, in A.J. van Loon (ed.), Developments in Sedimentology, Volume 65: Elsevier, Netherlands, 801 p.

- RICKARD, D. AND LUTHER III, G.W., 2007, Chemistry of iron sulfides: Chemical Reviews, v. 107, p. 514–562.
- ROBISON, R.A., 1964, Upper middle Cambrian stratigraphy of western Utah: Geological Society of America Bulletin, v. 75, p. 995–1010.
- ROBISON, R.A. AND RICHARDS, B.C., 1981, Larger bivalve arthropods from the middle Cambrian of Utah: The University of Kansas Paleontological Contributions, v. 106, p. 1–28
- SANSOM, R.S., 2016, Preservation and phylogeny of Cambrian ecdysozoans tested by experimental decay of Priapulus: Scientific Reports, v. 6, p. 32817.
- SANSOM, R.S., GABBOTT, S.E., AND PURNELL, M.A., 2010, Non-random decay of chordate characters causes bias in fossil interpretation: Nature, v. 463, p. 797–800.
- Schiffbauer, J.D., Wallace, A.F., Hunter Jr., J.L., Kowalewski, M., Bodnar, R.J., and Xiao, S., 2012, Thermally induced structural and chemical alteration of organic-walled microfossils: an experimental approach to understanding fossil preservation in metasediments: Geobiology, v. 10, p. 402–423.
- Schiffbauer, J.D., Xiao, S., Cai, Y., Wallace, A.F., Hua, H., Hunter, J., Xu, H., Peng, Y., and Kaufman, A.J., 2014, A unifying model for Neoproterozoic–Palaeozoic exceptional fossil preservation through pyritization and carbonaceous compression: Nature Communications, v. 5, no. 5754, p. 1–12, doi: 10.1038/ncomms6754.
- SCHMIDT-RHAESA, A., 2013, Priapulida, in A. Schmidt-Rhaesa (ed.), Handbook of Zoology, Gastrotricha, Cycloneuralia and Gnathifera: DeGruyter, Germany, p. 147–180.
- Schopf, J.W., Kudryavtsey, A.B., Agresti, D.G., Czaja, A.D., and Wdowiak, T.J., 2005, Raman imagery: a new approach to assess the geochemical maturity and biogenicity of permineralized Precambrian fossils: Astrobiology, v. 5, p. 333–371.
- SEILACHER, A., 1970, Begriff and bedeutung der Fossil-Lagerstätten: Neues Jarhbuch fur Geologie und Palaontologie Abhandlungen, v. 1970, p. 34–39.
- SHEN, C., PRAIT, B.R., AND ZHANG, X.-G., 2014, Phosphatized coprolites from the middle Cambrian (Stage 5) Duyun fauna of China: Palaeogeography, Palaeoclimatology, Palaeoecology, v. 410, p. 104–112.

- SKINNER, E.S., 2005, Taphonomy and depositional circumstances of exceptionally preserved fossils from the Kinzers Formation (Cambrian), southeastern Pennsylvania: Palaeogeography, Palaeoclimatology, Palaeoecology, v. 220, p. 167–192, doi: 10.1016/j. palaeo.2004.09.015.
- SPEAR, F.S. AND PYLE, J.M., 2002, Apatite, monazite, and xenotime in metamorphic rocks: Reviews in Mineralogy and Geochemistry, v. 48, p. 293–335.
- SUMRALL, C.D. AND SPRINKLE, J., 1999, Ponticulocarpus, a new cornute-grade stylophoran from the middle Cambrian Spence Shale of Utah: Journal of Paleontology, v. 73, p. 886–891.
- SUNDBERG, F.A. AND McCOLLUM, L.B., 2000, Ptychopariid trilobites of the lower-middle Cambrian boundary interval, Pioche Shale, southeastern Nevada: Journal of Paleontology, v. 74, p. 604–630.
- Vannier, J. and Chen, J.-Y., 2005, Early Cambrian food chain: new evidence from fossil aggregates in the Maotianshan Shale biota, SW China: PALAIOS, v. 20, p. 3–26.
- WILBY, P.R. AND BRIGGS, D.E.G., 1997, Taxonomic trends in the resolution of detail preserved in fossil phosphatized soft tissues: Geobios, Memoire special, v. 20, p. 493– 502.
- WILBY, P.R., BRIGGS, D.E.G., AND RIOU, B., 1996, Mineralization of soft-bodied invertebrates in a Jurassic metalliferous deposit: Geology, v. 24, p. 847–850.
- WILSON, L.A. AND BUTTERFIELD, N.J., 2014, Sediment effects on the preservation of Burgess Shale-type compression fossils: PALAIOS, v. 29, p. 145–153.
- ZHU, M., BABCOCK, L.E., AND STEINER, M., 2005, Fossilization modes in the Chengjiang Lagerstätte (Cambrian of China): testing the roles of organic preservation and diagenetic alteration in exceptional preservation: Palaeogeography, Palaeoclimatology, Palaeoecology, v. 220, p. 31–46.

Received 27 January 2017; accepted 29 July 2017.